Optical and Spin Properties of Nitrogen Vacancy Centers in Bulk and Nanocrystalline Diamond

By

Benjamin Kwasi Ofori-Okai

B.S. Chemistry
Yale University (2009)

SUBMITTED TO THE DEPARTMENT OF CHEMISTRY IN PARTIAL FULFILLMENT OF THE REQUIREMENTS FOR THE DEGREE OF

MASTER OF SCIENCE IN CHEMISTRY
AT THE
MASSACHUSETTS INSTITUTE OF TECHNOLOGY

FEBRUARY 2013

Signature of Author: _____
Department of Chemistry
December, 2012

Certified by: _____
Christian L. Degen
Assistant Professor of Chemistry
Thesis Supervisor

Accepted by: _____
Robert W. Field
Professor of Chemistry
Chairman, Committee for Graduate Students

Optical and Spin Properties of Nitrogen Vacancy Centers in Bulk and Nanocrystaline Diamond

by

Benjamin Kwasi Ofori-Okai

Submitted to the Department of Chemistry in September, 2012 in Partial Fulfillment of the Requirements for the Degree of Master of Science in Chemistry

ABSTRACT

The NV center is becoming a very hot topic in many areas of science, including, Physics, Chemistry, Biology, and Quantum Information. The Degen group has focused on a specific application of the NV center, namely scanning magnetometry. In my time in the group, I focused on building a microscope and studying NV centers in bulk and nanocrystalline diamond.

I began by building a confocal microscope which was capable of observing and determine single NV centers. I made measurements on the photon statistics of different defects to determine if they were single emitters or multiple emitters. I also made microwave frequency magnetic measurements to determine the spin properties of single NV centers by measuring their couplings to neighboring paramagnetic nuclei as well as to a spin bath. Through these efforts, I was able to successfully confirm that the microscope was capable of identifying and measuring single NV centers and their properties.

Lastly, I worked on the first steps of improving our understanding of NV centers in bulk diamond crystals. The goal of magnetometry involves putting the NV center as close to the diamond surface as possible. I made measurements that were aimed at studying the spin and coherence properties of the NV when it was within 10 nm of the diamond surface. These studies provided insight into the interactions of the NV center with the diamond surface.

Thesis Supervisor: Christian Degen
Title: Assistant Professor of Chemistry

Acknowledgments

It's a little odd to be writing out acknowledgments when I'm not yet done with grad school. But the writing of this thesis sort of closes a chapter on one part of my scientific career, and so I find it hard not to reflect on this time and thank some of the people who made it a special experience. Although that list is quite long, I feel I owe this thesis more specifically to the members of the Degen group. The rest will have to wait until my PhD thesis.

The first person who I need to thank is my former advisor, Christian. Christian was terrific. He was always willing to listen to my ideas as well as share his own. His excitement for his science made it easy for me to get excited and motivated to do my own work, and as I move forward in my graduate school career, I hope to take some of that with me. I'm not sure if I could have had a better start to graduate school had it not been for him. Being one of the top grad students in the lab on day one would have been a terrifying experience had it not been for the confidence that Christian had in me.

The people that I need to thank next are my former labmates Ye Tao, Brad Moores, and Kevin (Ting-Kai) Chang. The three of them were definitely a constant source of entertainment during my time in the Degen lab. Ye was a great source motivation for me, both inside and outside the lab. His work ethic was infection and this often made it easy to focus when work had to be done. Even with that, I can say that I was happy to learn that there was more to him as we frequented the gym for squatting and cleaning sessions. I can't say that I've been good about going since Ye left, but I hope that when I see him again I'll be stronger than I was when he left.

Brad was the last one to join the group, but he was certainly a welcome addition to our forces. He was great for conversations, were they about science, trivia, pop-culture, just about anything. Brad has a great way of forcing me to make sure that I believe what I'm saying, because there was never any way that I could have a meaningful discussion with him otherwise. Through countless discussions with him about NV centers, YIG crystals, our goals in science and our professional careers, I felt like I really got to grow. And when it wasn't that, it was hanging out at the Asgard playing trivia or listening to music and just enjoying time in the lab.

Lastly, there was Kevin Chang. Kevin was sort of like my partner in crime in the lab, and more than just because our projects were closely related. Whenever I needed a laugh, I could always count on Kevin to be there with a ridiculous youtube video, or a quote from one, or

anything else to help put me in a better mood. Kevin made being in either the lab or the office (especially the office) a great distraction from work. And when work needed to get done, Kevin was always a great source of discussion, and always asked useful and often thought provoking questions. I don't think there was a single day that went by when I wasn't able to enjoy work because of Ye, Brad, or Kevin. Thank you all, for making my time in the Degen lab so enjoyable. I know you're all doing spectacular things now and will continue to do so in the future.

Table of Contents

Chapter 1: Introduction and Background

The development of new kinds of spectroscopy and microscopy has been an ongoing challenge in science. The advances that have come from new spectroscopic techniques have allowed us to probe systems on a more fundamental level. Magnetic resonance spectroscopy in particular has become a powerful tool for analyzing molecules because of its high sensitivity to different nuclei and different chemical environments.

This thesis is the result of an early attempt at developing a new technology, namely diamond based nanoscale magnetometry, through the combination of different older spectroscopic methods. It will be broken up into three chapters. This first one discusses the background of the NV center and lays out a formalism for describing it's electronic and spin states. The next chapter describes the optical setup and also presents the early work that I did to characterize my setup and to find and distinguish NV centers. The last chapter focuses on the work that I did to study very shallow NV centers in bulk diamond

1.1 Background of the nitrogen-vacancy center

The nitrogen-vancancy (NV) center has recently become a high profile candidate for many different solid state applications, ranging from solid state quantum computing to magnetometry. It falls into a class of point defects in diamond. It is generated by removing two adjacent carbon atoms and replacing one of them with a nitrogen while leaving the other site vacant. The NV defect has been known for quite some time [Davies1976]. Its electronic properties have been studied in bulk diamond where the concentration of nitrogen is quite high. Only recently has it been possible to study single NV centers and study the two different charge states because of the increase in the prominence of different optical microscopies [Gruber1997, Mainwood1997, Gaebel2005, Rittweger2009].

The NV center comes in different varieties [Mita1996]. The most often studied forms are the negatively charged NV center, usually referred to as NV^- or just the NV center, and the neutral form the NV center, referred to as NV^0. When the defect forms, the three carbon atoms adjacent to the vacancy donate one electron each into the vacancy, the nitrogen donates two electrons coming from the non-bonding pair for a total of 5 electrons. In the case of the NV^-, the extra electron comes from another site in the lattice, often coming from other nitrogen impurities

that are present in the lattice [Manson2006]. There are other positively charged forms in addition to these, but they will not be mentioned here.

1.2 Physical Structure

The Nitrogen-Vacancy (NV) center is a point defect in the diamond crystal structure. The pure diamond crystal structure is a slightly modified version of the of a face-centered cubic (FCC) lattice. Unlike the FCC lattice, the diamond lattice has a two atom basis, meaning that each lattice point actually references two atoms. Mathematically this is done by placing one of the atoms directly at each lattice point and displacing the other atom by $\frac{a}{4}$ in the x, y, and z direction, where a is the lattice constant of diamond, 0.357 nm [AshcroftMermin1976] Physically, this gives two FCC lattices, which are offset by one another by exactly $\frac{a}{4}$ in x, y and z. The NV defect in diamond is generated by removing two adjacent carbon atoms in the lattice and replacing one of them with nitrogen and leaving the other site vacant.

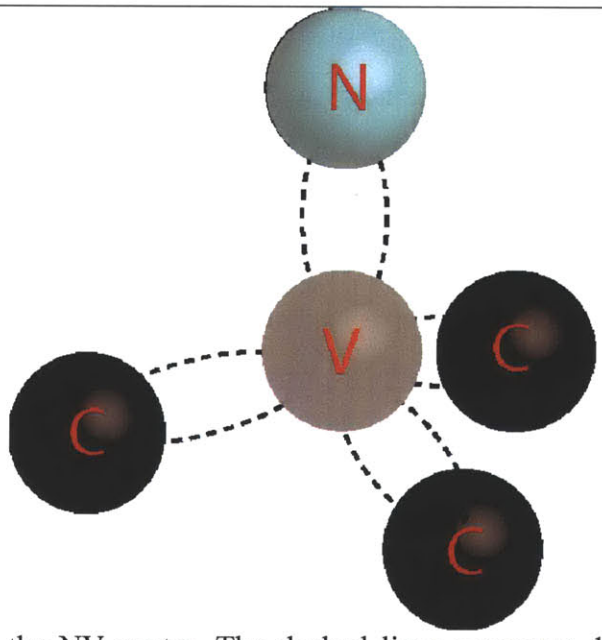

Figure 1.1 A cartoon of the NV center. The dashed lines represent dangling bonds which all overlap in the vacancy. The carbon atoms each contribute one electron, the nitrogen atom contributes two electrons, and one more electron comes from other lattice defects to generate the negatively charged NV center.

As mentioned above, the NV center has been shown to exist in two different electronic forms [Mita1996]. One form is the neutral form, referred to in the literature as NV^0, and a negatively charged form, referred to as NV^-. In almost all cases in this work, the term NV or NV center will be used to refer to its negatively charged form, and when necessary a distinction will be made between the two. The electrons in the NV center come from the dangling sp^3 bonds of the carbon atoms and from the lone pair of electrons located on the nitrogen. The neutral form contains 5 electrons and the negative charged state has 6. In the case of the negatively charged form, the extra electron may come from other nitrogen atoms found in the lattice, as well as other defect sites [Gali2008, Gali2009]. The wavefunctions are highly localized around the defect and as such it is possible to think about the NV as an artificial atom within the diamond host.

1.3 Group Theory Treatment of Electronic Orbitals

When describing molecular and solid state systems, it is useful to consider the symmetry of the system in determining its quantum mechanical properties. The reason is because if a molecule posses some kind of symmetry element that means it can be rotated or reflected in such a way as to look unchanged. Consequently, characteristics of that molecule must also transform in ways that make it appear as though nothing has changed. Knowing what symmetry elements a specific system has can provide useful information in determining whether or not certain spectroscopic transitions can be observed. Two of the most commonly used examples are bond vibrations and electronic structure. By considering the symmetry of a given molecule, it is possible to determine that certain vibrational modes will be Raman active and that other modes will be IR active. Group theory can also be used to determine electronic structure, because the wavefunctions for a molecule must also transform with the appropriate symmetry.

The formalism for this analysis comes from group theory. [Cotton1990, Kettle1995, Bernath2005]. In group theory, molecular systems are described by the symmetry elements that system has. There are 5 symmetry elements that a given system can possess, each of which is represented by a different symbol: a mirror plane (σ), an n-fold rotation axis (C_n), an n-fold improper rotation axis (S_n), an inversion center (i), and finally the identity (E). A given system possesses one or more of these elements, and the set of all symmetry elements that a system possesses defines its point group. Point groups are represented by different symbols that indicate something about the number and type of symmetry elements that make up the point group.

Although there are an extremely large number of molecules and systems, the total number of point groups in 3D is finite and can be tabulated. Once the point group of a system is known, a character table can be used to learn what unique symmetry elements it has.

Symmetry elements can also be represented mathematically using matrices. This can be thought of intuitively because symmetry elements transform one point in 3D space to another point. For example, a mirror reflection across the xy-plane will take a point at +z to -z. This naturally lends itself to writing down

$$\sigma_{xy} = \begin{bmatrix} 1 & 0 & 0 \\ 0 & 1 & 0 \\ 0 & 0 & -1 \end{bmatrix}$$

Matrices for all symmetry elements can be generated by carefully tracking how the points move under the corresponding symmetry operation. When considering molecules with multiple atoms, it is not sufficient to consider only how the coordinates change -- one must also be aware of how the atoms move as well. This means that for a molecule with N atoms, the matrix for a symmetry transformation will be 3N x 3N in dimension. While this might seem like it adds complexity to the group theory formalism, there is a simple way of keeping track of everything will be described later.

The ideal diamond lattice depicted above has tetrahedral symmetry, and belongs to the point group T_d. The T_d point group has a number of symmetry elements, such as C_3 axes, mirror planes, and improper rotation axes. At the NV center, the substitution of the nitrogen and the presence of the adjacent vacancy breaks the tetrahedral symmetry of the diamond lattice. Consequently, its symmetry is reduced changing the point group from T_d to C_{3v}, which also reduces the number of symmetry elements. The character table for C_{3v} is shown below:

Table 1.1: Character Table for C_{3v} Point Group

	E	2 C_3	3 σ_v		
A_1	1	1	1	z	x^2+y^2
A_2	1	1	-1	R_z	
E	2	-1	0	(x,y). (R_x, R_y)	(x^2+y^2, xy) (xz yz)

The top row of the character table shows the symmetry elements for the point group. In this case they are the identity, two three-fold rotations, and three mirror planes. The subscript v on the

mirror planes signifies that the mirror planes are parallel to the highest n-fold rotation, in this case the C_3 axis. Note that in this case there is only one C_3 axis. The 2 represents the fact that the rotation around this axis can be either clockwise or counter-clockwise. Additional C_3 axes would be marked as C_3', C_3'', etc. The other rows give the irreducible representations for the C_{3v} point group. The irreducible representations in essence make up the basis set for a particular point group. Properties like the dipole moment must transform like irreducible representations. The general mathematics that are used to formalize them can be found in the references listed above, and will be omitted here. Instead, I will describe how the irreducible representations work for this particular case. In short, there are 3 representations that describe the C_{3v} basis. The A_1 representation has a character of 1 under each E, C_3, and σ_v. This means that the A_1 representation is symmetric with respect to the molecule. Consequently anything in the NV center that transforms like A_1 must be this way as well. For example, if there is a wavefunction that has A_1 character, it must be symmetric with respect to all three transformations in C_{3v}. In this case, such a wavefunction would be cylindrically symmetric. The A_2 representation has a character of 1 under E, and C_3, but has a character of -1 under σ_v. This means that it is symmetric under the E and C_3 transforms, but changes sign under mirror reflection. Examples of shapes that transform like A_1 and A_2 are shown in figure 1.2.

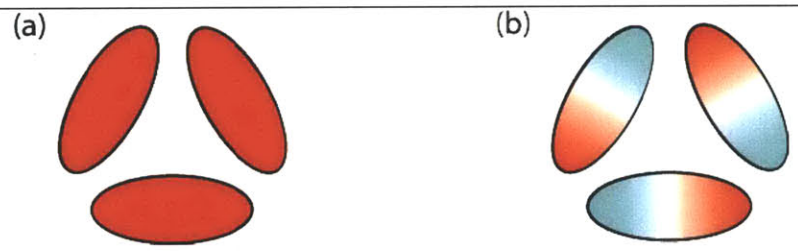

Figure 1.2: Examples of shapes that possess all the symmetry elements of C_{3v}. The signs of the shapes are given by the blue and red colors. Red indicates a positive sign while blue indicates a negative sign. (a) In this situation, the sign of the shapes remains unchanged under each of the symmetry operations of C_{3v} and consequently this has the A_1 type symmetry. (b) Here, there is no sign change under the C_3 rotations, but because half of each oval is now of opposite sign, the mirror reflections now cause a sign change to occur, meaning that this structure now possess A_2 symmetry.

The E representation is very different from either the A_1 or the A_2 representations. The fact that is has a character of 2 under the E symmetry element means that it possesses a double-

degeneracy, and anything that transforms like E will be doubly degenerate. This degeneracy can be lifted by distorting the lattice in some way as to break the C_{3v} symmetry.

Having discussed that, we can now use what we know to get a picture of what the single-electron orbitals for the NV center look like. To do this, we first realize that these orbitals are going to be constructed from the dangling bonds that go into the NV center. Next, we pose the following question: for each of the symmetry operations in C_{3v}, how many of the bonds stay in exactly the same place? Another way to think of this is as follows: if we could somehow tag each of the dangling bonds with a label -- a, b, c, and d -- under each symmetry operation how many of the labels stay the same? For E, all four stay the same. For the C_3 rotation, only one of them will stay the same, and for the σ_v, 2 remain the same. From this, we can say that the wavefunctions for NV have a representation, Γ, which has characters of 4, 1, and 2, for E, C_3, and σ_v.

	E	$2\,C_3$	$3\,\sigma_v$
Γ	4	1	2

Looking at this we can see that it does not match up with any of the irreducible representations for C_{3v} encountered before. This just means that Γ itself is not an irreducible representation, but that it can be described as a sum of irreducible representations. Checking which irreducible representations are present is done by taking the characters of those irreducible representations and seeing that they sum to the representation that was generated. In this case, $\Gamma=2A_1+E$, as can be seen through the following

	E	$2\,C_3$	$3\,\sigma_v$
$2\,A_1$	2	2	2
E	2	-1	0
Γ	4	1	2

This analysis shows that there are 4 different single-electron state, two of which transform with A_1 symmetry, labeled as $a_1(1)$ and $a_1(2)$, and a doubly-degenerate set of states that possesses E symmetry, which are labeled e_x and e_y. Through the use of DFT calculations [Gali2008, Goss1996], as well as through considerations of the electron-ion interactions [Lannoo1981], the states can be ordered from lowest to highest as follows: $a_1(1) < a_1(2) < (e_x,e_y)$.

The last step of our analysis is to see what the multi-electron states look like. To do this, we must first populate the single electron states and determine the representation of that state. In the ground state, the six electrons of the NV center will occupy the the orbitals as $[a_1(1)]^2[a_1(2)]^2(e_x,e_y)^2$. The overall representation of this new state is obtained by multiplying the characters of the partially filled states, in this case e_x and e_y. This means that for the multi-electron state, the representation, Γ_M, is given by

	E	$2\,C_3$	$3\,\sigma_v$
Γ_M	4	1	0

This can be broken down into irreducible representations as before.

	E	$2\,C_3$	$3\,\sigma_v$
A_1	1	1	1
A_2	1	1	-1
E	2	-1	0
Γ_M	4	1	0

From this analysis, we conclude that the there are four possible multi-electron states, one of which transforms as A_1, one which transforms as A_2, and a doubly-degenerate pair that transforms as E [Manson2006]. Also of interest is the excited state configuration of the NV center. The first excited state is obtained by promoting an electron from the $a_1(2)$ single electron state to either the e_x or e_y states, generating the following configuration: $[a_1(1)]^2[a_1(2)]^1(e_x,e_y)^3$. The representation of this state is E, as the partially filled states are of A_1 and E type.

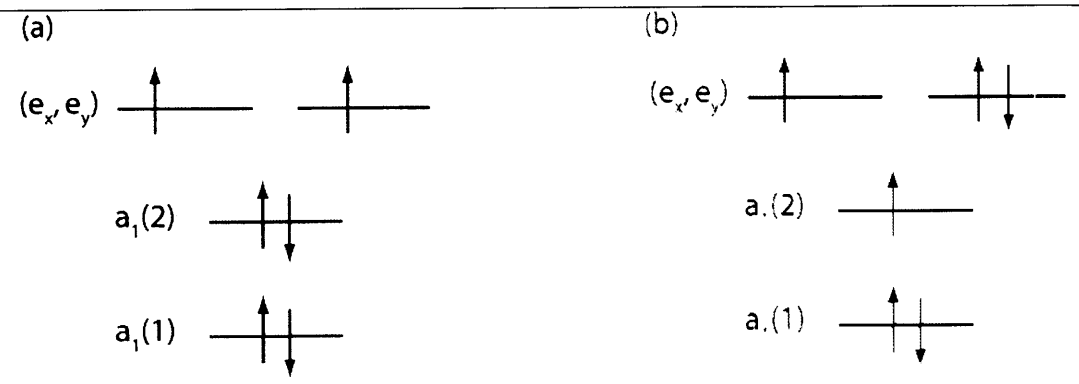

Figure 1.3: Filled orbitals for the (a) ground state and (b) first excited state of the NV center.

Finally, we consider the electrons themselves, which have thus far been omitted from the discussion. The spin states for this effectively two-electron system can be described as being either singlet states or triplet states:

$$|T\rangle = \begin{cases} |\alpha_1\alpha_2\rangle & m_s = -1 \\ |\alpha_1\beta_2\rangle + |\beta_1\alpha_2\rangle & m_s = 0 \\ |\beta_1\beta_2\rangle & m_s = +1 \end{cases}$$

$$|S\rangle = |\alpha_1\beta_2\rangle - |\beta_1\alpha_2\rangle \quad m_s = 0$$

The two electrons in this system couple together to from either triplet or singlet states. The ground state configuration can be deduced by considering the effect of the Coulomb interaction between the electronic states [Maze2011]. By applying the Hund's Rule of maximum spin multiplicity, which states that the ground state is the state with the highest spin multiplicity (2S+1), the ground state is determined to be a triplet state. In addition, because the overall wavefunction must be antisymmetric, since the electrons are fermions, the spatial configuration of the electrons should be antisymmetric. This predicts that the NV ground state is overall $^3A_2$. For the work I will discuss, the most relevant states for discussing throughout this work are the ground state, which is represented as a $^3A_2$ state, and the first excited state which is a ^3E state [LenefBrown1996, LenefRand1996]. Additionally, there are singlet levels that are present between the ground and excited states. However, there is currently much contention over the ordering of the energies between them, and such discussions are beyond the scope of this thesis. I therefore assume that there is one $^1A_1$ state between the ground and excited state. The full energy level diagram is given below.

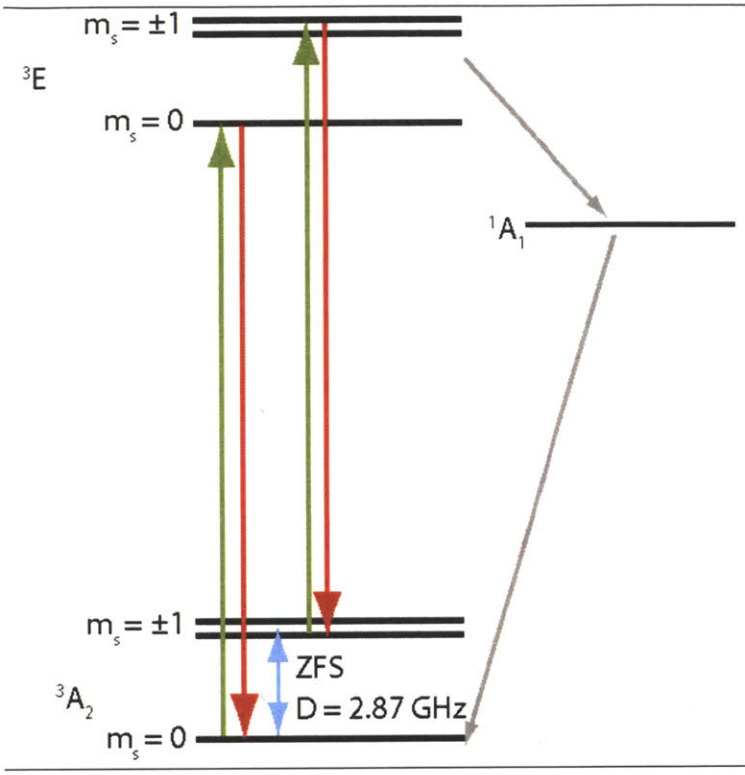

Figure 1.4. Schematic of the energy level diagram in the negatively charged NV center. The ground and first optically accessible excited state are both triplet states, with the $m_s = 0$ being split from the $m_s = +1$ and -1 states. The ground state zero-field splitting, ZFS, is given by D = 2.87 GHz. There is also a singlet level which can be accessed through spin-orbit coupling.

References:

[AshcroftMermin1976] Ashcroft, N.W., Mermin, N.D., *Solid State Physics*, Brooks/Cole, Belmont, CA (1976)

[Bernath2005] Bernath, P.F., *Spectra of Atoms and Molecules*, Oxford University Press, New York, NY, 2005

[Collins1983] Collins, A.T., Thomaz, M.F., et al., "Luminescence decay time of the 1.945 eV centre in type Ib diamond", J. Phys. C, Solid State Phys. 16(11), 2177–2181 (1983).

[Cotton1990] Cotton, F.A., *Chemical Applications of Group Theory*, John Wiley & Sons: New York, 1990.

[Davies1976] Davies G., Hamer, M.F., "Optical Studies of the 1.945 eV Vibronic Band in Diamond." Proc. R. Soc. Lond. A 348, 285-298 (1976)

[Gaebel2005] Gaebel, T., et al. (2005). "Photochromism in single nitrogen-vacancy defect in diamond." *Applied Physics B*, *82*(2), 243–246 (2005).

[Gali2008] Gali, A., Fyta, M., Kaxiras. E., "Ab initio supercell calculations on nitrogen vacancy center in diamond: Electronic structure and hyperfine tensors." Phys. Rev. B, 77:155206 (2008)

[Gali2009] Gali, A., "Identification of individual ^{13}C isotopes of nitrogen-vacancy center in diamond by combining the polarization studies of nuclear spins and first principles calculations." Phys. Rev. B, 80(24):241204 (2009)

[Goss1996] Goss, J.P., et al. "The twelve-line 1.682 ev luminescence center in diamond and the vacancy-silicon complex." Phys. Rev. Lett., 77:3041 (1996)

[Gruber1997] Gruber, A., Drabenstedt, A., et al., "Scanning Confocal Optical Microscopy and Magnetic Resonance on Single Defect Centers" Science 276(5321), 2012–2014 (1997).

[Kettle1995] Kettle, S.F.A., *Symmetry and Structure*, John Wiley & Sons, Inc., West Sussex, 1995

[Lanoo1981] Lannoo, M., Baraff, G.A., Schlüter. M., "Self-consistent second-order perturbation treatment of multiplet structures using local-density theory." Phys. Rev. B, 24(2):943–95 (1981)

[LenefBrown1996] Lenef, A., et al., "Electronic structure of the N–V centre in diamond: Experiments", Phys. Rev. B 53(20), 13427–13440 (1996).

[LenefRand1996] Lenef, A., Rand, S.C., "Electronic structure of the N–V centre in diamond: Theory", Phys. Rev. B 53(20), 13441–13455 (1996).

[Loubser1978] Loubser, J.,Vanwyk, J.A., "Electron–spin resonance in study of diamond" Rep. Prog. Phys. 41(8), 1201–1248 (1978)

[Mainwood1997] Mainwood, A., Stoneham, A.M., "The vacancy (V – 0, V+, V–) in diamond: The challenge of the excited states and the GR2–GR8 lines", in: Proceedings of the 13th International Conference on Defects in Insulating Materials – ICDIM 96, Vol. 239-2 (1997)

[Manson2006] Manson, N., Harrison, J., Sellars, M. "Nitrogen-vacancy center in diamond: Model of the electronic structure and associated dynamics." *Physical Review B*, *74*(10), 1–11. (2006)

[Maze2011] Maze, J.R., et al, "Properties of nitrogen-vacancy centers in diamond: the group theoretic approach" New Journal of Physics **13**, 025025 (2011)

[Mita1996] Mita, Y., "Change of absorption spectra in type-Ib diamond with heavy neutron irradiation", Phys. Rev. B 53(17), 11360–11364 (1996)

[Rittweger2009] Rittweger, E., et al., (2009). "STED microscopy reveals crystal colour centres with nanometric resolution," Nature Photonics, *3*, 144-147. (2009)

Chapter 2 Optical Set-up Details and Preliminary NV Experiments

2.1.1 Background of Confocal Microscopy

Since the late 1980s [Minskey1988], the use of confocal microscopy has led to the growth and development of many different fields in science. In a sense, confocal microscopy can be thought of as the most inefficient way of taking a picture. A confocal image is built by going to a certain spot and shining light onto that one spot. If something in that spot is excited and fluoresces, the microscope collects the light from that one particular place and records the amount of light. Next, the sample is moved a tiny amount and light is collected from this new point. By continuously moving, a confocal image is built. The use of high quality optical elements, high precision stages, as well as spatial and spectral filters enables confocal microscopy to generate very nice, high resolution images. This technique has found many different applications in biology, chemistry, and physics [Moerner2002], and of course on NV centers [Gruber1997].

The theory of confocal microscopy can be thought of from a ray optics perspective or a fourier optics perspective. The explanations that I give here borrow from both and utilize different formalisms developed in Born and Wolf [BornWolf1999], Saleh and Teich [SalehTeich2007], Goodman [Goodman2004], and Haus [Haus1984]. There are four major components to the confocal microscope: the coherent light source, the objective lens, the dichroic mirror, and the pinhole in the image plane. The light source, in my case a laser, provides optical excitation to a small portion of the sample. The objective, which can be thought of as a lens with a very high numerical aperture, or NA, focuses the incident light to a very small region of space where the sample is located. The dichroic mirror reflects light of a specified wavelength while transmitting light of a different wavelength. Finally, the pinhole in the image plane spatially isolates the light that comes back from the sample.

A general schematic of the confocal microscope that I used in my experiments is show in figure 2.1. In this case, light from the laser was directed into the back of the objective. As stated above, the objective can be thought of as a lens with a very high NA. The NA of a lens is given by the following formula:

$$NA = n\sin\left(\arctan\left(\frac{D}{2f}\right)\right) \tag{2.1}$$

In this case, n is the index of refraction of the medium, f is the focal length of the lens, and D is the diameter of the beam when it passes through the lens, which obviously cannot exceed the diameter of the lens itself. In the limit that the focal length of the lens is much larger than the diameter of the beam, the final part of the previous equation can be simplified to read

$$NA = n\sin\left(\arctan\left(\frac{D}{2f}\right)\right) \approx n\frac{D}{2f} \tag{2.2}$$

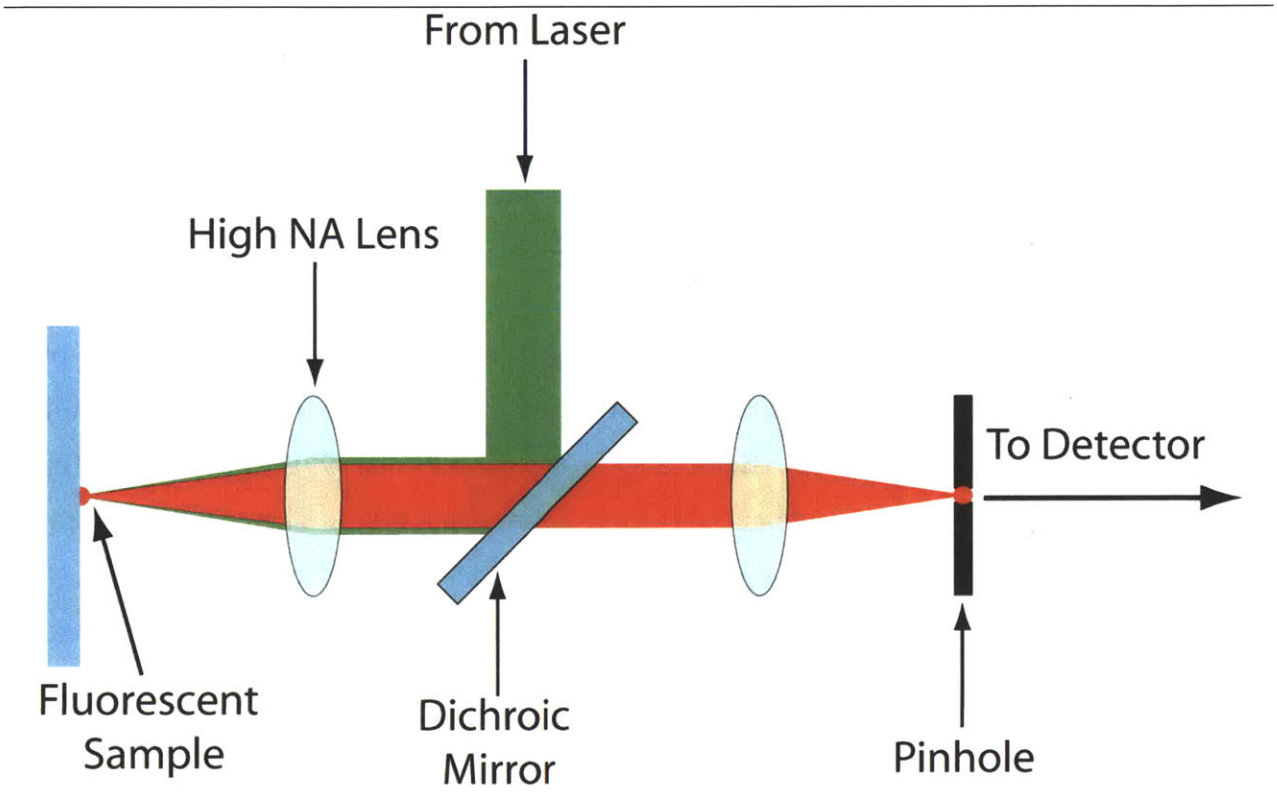

Figure 2.1. Cartoon representation of confocal microscope used in NV experiments. This figure also serves to illustrate the essential features of a confocal microscope.The light from the laser is reflected off the dichroic mirror and focued using the high NA (ie. objective) lens. The sample sits at the focus and when excited, fluoresces. This fluorescence is collected by the lens, and passes through the dichroic mirror, because the wavelength of the emitted light is shifted in frequency from the excitation. It is this focused through a pinhole to spatially filter the beam

The use of a high NA lens is important because the NA it is related to the minimum spot size of the beam after it has been focused through the objective. For light with wavelength λ, the minimum spot size of the beam, d_0 is given by

$$d_0 = \frac{0.61\lambda}{NA} \tag{2.3}$$

and so consequently the larger the NA, the smaller the spot size.

The sample itself is ideally placed on some kind of substrate – glass, for example – and sits at the focal plane of the objective. In order for the sample to be detected through the microscope, it must fluoresce after absorbing light from the excitation source. Typically, the emitted light is at a longer wavelength than the excitation, and can be spectrally separated by the dichroic mirror. In the experiments that I will discuss, the dichroic mirror reflected the excitation beam and transmitted the reflected light, but obviously this need not be the case.

The emitted light is then focused through another pinhole to spatially filter light that is in the focal plane of the objective. A rigorous explanation of this can be understood through the use of Fourier optics, but a simple way of understanding what is going on here is by thinking of this as a two-lens imaging system. Such an imaging system consists of two lens with focal lengths f_1 and f_2 that are spaced apart by $f_1 + f_2$. The reason that this is defined as an imaging system is because if you place a point at height h_1 a distance f_1 away from the first lens, that point will be mapped onto a point with height $h_2 = h_1\left(\frac{f_2}{f_1}\right)$ at a distance f_2 away from the second lens. A cartoon representation is shown in figure 2.2. In this way, the focal plane of objective and the focal plane of the lens focusing the emission are said to be equivalent or conjugate planes. There are two important cases to consider: light that is coming the focus of the objective and light that is not. Light that is at the focus is directly in the middle of the lens, and effectively this means that $h_1 = 0$. This means its height, h_2, at a distance f_2 from the second lens is also zero. If the pinhole is correctly aligned, it lies along the center of the lens, and so only light from the focus makes it through.

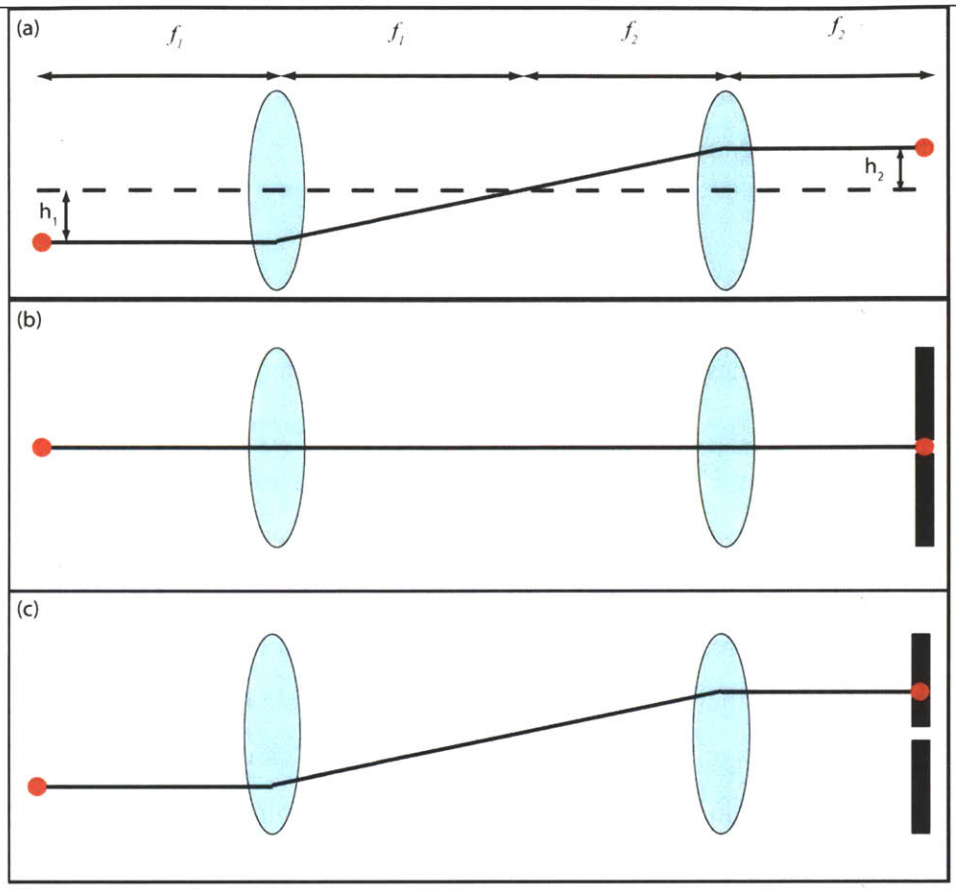

Figure 2.2. (a) Illustration of a two lens, 4f imaging system using ray-tracing optics. In this case, the red spot at height h_1 is mapped onto a height h_2. The ratio $\frac{h_2}{h_1} = \frac{f_2}{f_1} = M$ is the magnification of the imaging system (b) When the rays originate right along the center axis of the imaging system, there is no change in height at all. Consequently, when the pinhole is aligned properly, this beam passes through the open aperture. (c). When the rays originate off-axis, the corresponding spot after the second lens is not in the open aperture and the beam is blocked.

The resolution of the microscope can be quantified through the point spread function, PSF, of the imaging system. The point spread function is a measure of the spatial intensity distribution of the beam, and this function varies both laterally, along the beam propagation axis, and radially, in the plane perpendicular to the beam propagation axis, depending on the input. For the case of a collimated beam entering the back of the of the objective, the radial distribution of the point spread function is given by

$$PSF = P(r) = 2\left[\frac{J_1(\alpha r)}{\alpha r}\right]^2 \tag{2.4}$$

where $\alpha = \frac{4\pi NA}{\lambda}$ and the function $J_1(x)$ is the Bessel function of the first kind. To build an intuition for what the point spread function is, think of it as the response of the imaging system to an infinitely small emitter at the focal point of the objective. In the ideal world an infinitely small emitter maps on to an infinitely small point. However, because a lens with a finite NA cannot collect all the emitted light, this turns out to not be the case. In this case, an infinitely small emitter returns an intensity distribution given by the equation above. The confocal image, $I(x,y)$, that is actually obtained by scanning over the sample can be determined by taking the convolution of the PSF with the sample. In math, this would be represented as

$$I(x,y) = \int_{-\infty}^{\infty}\int P(x-x_0, y-y_0) f(x_0, y_0) dx_0 dy_0 \tag{2.5}$$

where $f(x_o,y_o)$ represent the spatial distribution of the fluorescent spots on the slide. For the case of the NV center in the confocal microscope, the NV center itself is much smaller than dimensions of the PSF, and consequently, it can be approximated as a Dirac delta function. Using this, the above equation can be simplified to say

$$I(x,y) = P(x_0,y_0) \tag{2.6}$$

which is equivalent to shifting the point spread function to the location of the NV center.

There are a few experimental considerations that should be discussed before continuing. In the ideal case, the dichroic mirror does a perfect job of reflecting some wavelengths and transmitting others, but this is obviously not so. There is always some imperfection in the dichroic mirror and some amount of excitation light which makes it to the detector. While dichroic mirrors can be designed to have an optical density of 6, meaning that for every 10^6 photons that hits it only 1 gets through, the fact remains that often there are many photons at the excitation wavelength that are reflected and do pass back through the dichroic mirror. Additionally, the detectors used in these measurements are often sensitive to single photon numbers, and so these can be measured. Although this seems like it should be a huge problem, it turns out not to be the case. When aligning the microscope, I often used a spike in counts that

came from the reflections at the interface between glass slide and air to determine whether or not I was close to where I expected there to be NV centers.

2.1.2 Stationary beam version

During the course of these experiments, two different versions of the microscope were used. Both of these versions are represented schematically in figure 2.3. In both cases, the set up can be described in three different regions. The first region was used for beam modulation and beam control. A continuous wave, CW, diode laser which emitted 532 nm (CNI DPSS MGL-III-532 LD Pumped All-Solid-State Green Laser) light provided a source of optical excitation. The laser works by using the emission from a neodymium yittrium-aluminum-garnet (Nd:YAG) crystal and frequency doubling it. This produced a CW 532 beam. An Omega Optical laser line filter (XLK 08) which passes only 532 nm light and blocks any stray 1064 nm light was placed after the output of the laser to make sure that no 1064 got through. When the beam exits the laser it was reflected off several mirrors and eventually focused into the acousto-optic modulator, or AOM (Crystal Technologies AOMO 3200-144). As discussed later, there were a set of experiments that required the laser to be pulsed on and off on the nanosecond timescale, and for this reason it was necessary to modulate the beam intensity using the AOM, which has a rise time of 10 ns. When the AOM was turned on, the input beam was diffracted and the first-order diffraction could be spatially selected with the use of a circular aperture, as shown in figure 2.3. After this, the beam was magnified using a 4x telescope before it was coupled it into a single mode fiber using a cage system from Thorlabs (KT110 - Fiber Launch System). The input beam was focused using a 10x objective (RMS10X - 10X Olympus Microscope Objective) into a single mode fiber. There are two purposes for using the single mode fiber. The first is that it effectively decouples any alignment in this area from subsequent areas of the set up. Consequently, realignment can be done in the first part of the setup without affecting the alignment later, making it easier to add or remove elements. The second is that the use of a single mode fiber produces a beam with a nice spatial profile.

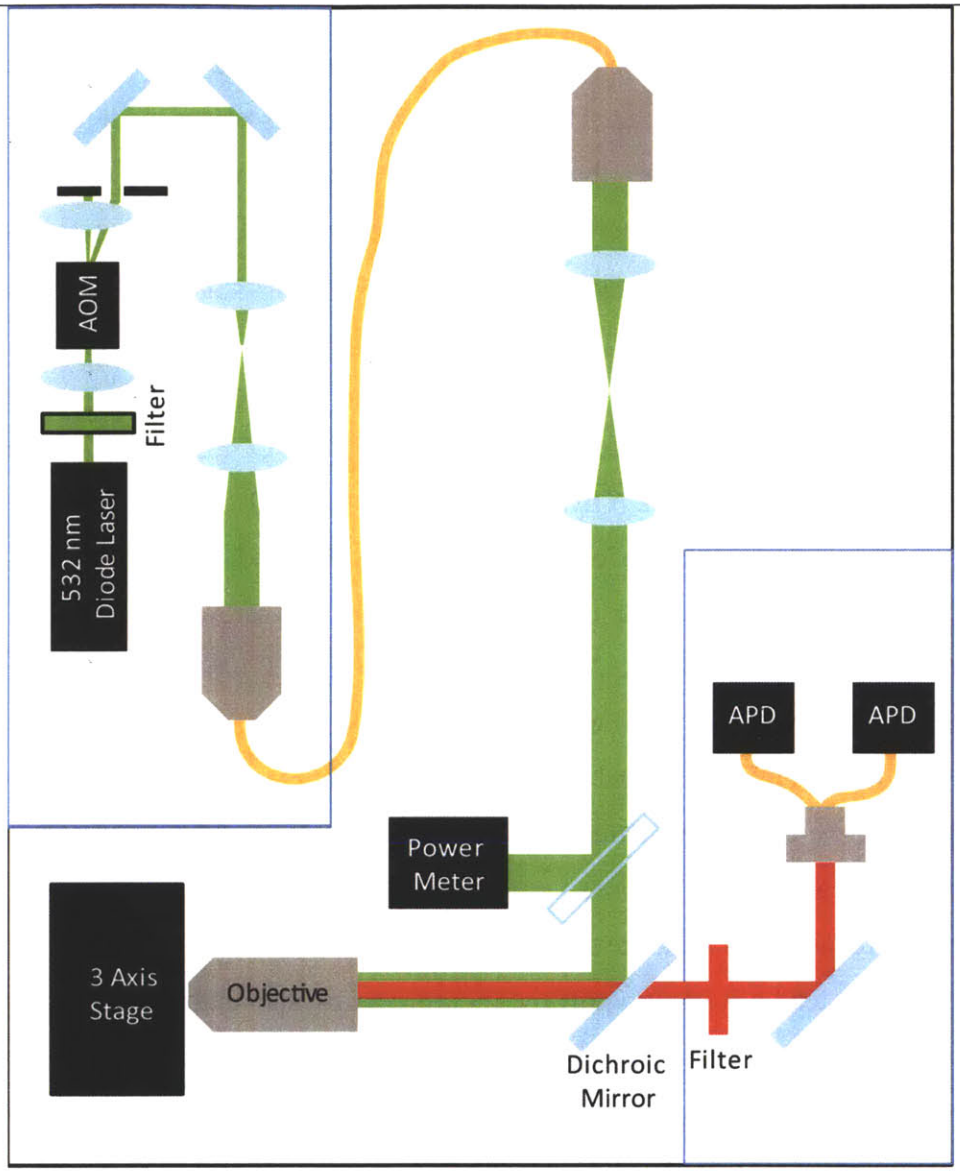

Figure 2.3. Schematic of optical setup used in experiments.

The second region of the setup was where the scanning of the sample happened. In both versions of the setup, the beam was recollimated after exiting the single mode fiber using a recollimator (F280FC-A from Thorlabs) and pair of lenses. Next a Thorlabs (BP108 1") 8:92 :: R:T pellicle beamsplitter was used to send 8% of the total power to a power meter to enable simultaneous measurement of signal intensity and power if necessary. The beam then reflected off the Omega Optical dichroic mirror (XF2016 560 DCLP) and was directed towards a 45-degree mirror, which reflected the beam so that it is propagating perpendicular to the plane of the optics table. A rectangular aluminum breadboard with a whole milled through its center was

elevated using four 1.5" posts from Thorlabs (Thorlabs P8 Ø1.5" Mounting Post, Length=8", 1/4"-20 Taps). The posts were mounted to the table and this provided a raised platform where the sample and the objective were located. The 45-degree mirror was placed such that it was roughly centered on the milled hole so that the beam passed through the center of the hole. To the underside of the breadboard a Newport 3-axis stage (462-XYZ-SD) was mounted such that the adjustable face was directed towards the opening. A custom made angle piece was mounted to the Newport stage. One side of the angle bracket had holes drilled to match the Newport stage. The other portion of the bracket was fitted with a lens tube with internal SM1 threads. The high NA objective lens, either an air objective (Olympus UPLSAPO 40X2, 40x air objective, NA 0.95) or an oil-immersion objective (Olympus UPLFLN 100XO2, 100x oil objective, NA 1.30, WD 0.20 mm), was screwed into the lens tube using an SM1 to RMS adapter. The sample itself sat on a custom made aluminum sample holder, which was then screwed into a 3-axis piezostage (PI P-527.3CL) capable of translating 200 μm in X and Y and 20 μm in Z when operating in the closed loop mode. In this configuration, the objective and the beam remained stationary while the sample was translated in the x and y directions. The sample could be brought in and out of focus by adjusting the objective manually using the 3-axis Newport stage, and then using the piezostage for fine scanning.

When the focused beam hit the sample and it and fluoresced, the light traveled back along on the same path. Instead of reflecting off the dichroic mirror the majority of fluoresence passed through it because the wavelength has been shifted and entered the final portion of the set up where the signal detection happened. The back-scattered beam wass split by a 45:55 :: R:T pellicle beam splitter (Thorlabs BP145B2) . This sent 45% of the light toward one detector and transmitted 55% to the other. The two beams were reflected off two mirrors and then focused into single mode fibers using Fiber Port Collimators (Thorlabs PAF-X-18-B). The single mode fibers were connected to avalanche photodiodes, or APDs, (PerkinElmer SPCM-AQRH-13-FC) via single mode fibers. The APDs were capable of counting single photon evens and converting them to electrical signals in the form of TTL pulses which could be detected by connecting the output of the APDs to a National Instruments Shielded Connector Block (NI DAQ BNC 2121), which was connected to a National Instruments Digital Counter Card (NI DAQ PCI-6602). In some cases the transmitted beam was focused through a lens to focus onto a CCD (Waton WAT 120N+) which was used for alignment and could be used, in principle, for wide-field imaging.

The majority of the setup was fairly straightforward to align. One particularly challenging area was the alignment of the fiber port collimators, and so I will briefly summarize the procedure that I used here. The first step was to align the 532 nm almost to the point of where the objective was located. Instead, however, I would send the beam off several mirrors just to have the beam propagate a significant distance. In order to set up the FiberPort collimators, what worked best was to use another fiber coupled laser source at ~630 nm (Thorlabs S1FC635 Fabry-Perot Benchtop Laser Source, 635 nm, 2.5 mW, FC/PC) and plug that into the back of the fiber port. This allowed me to correctly position the lens in the fiber port to make sure that the beam was collimated. It also helped to guarantee that the incoming beam, which should be collimated as well, would couple into the single mode fiber with fairly high efficiency. After that had been done, I would then use this as a source of 630 nm light, which would pass through the dichroic, and I would overlap the 532 nm and the 630 nm beams over a long distance. This procedure would be done with both of the fiber ports to ensure that they were both aligned fairly accurately. Once they were close, the 532 nm light alone was sufficient to align into the back of the objective. Even with this, it was necessary to make fine adjustments, which I will describe in later sections.

2.1.3 Stationary sample version

The two versions of the setup were identical in the first region. The differences come in the last two regions where the sample was scanned and where the signal is detected. In this version of the setup, after the beam was reflected off a dichroic mirror, it was directed to a set of scanning galvano mirrors (Cambridge Technologies Galvano Scanning System). In order to move the scanning mirrors, a voltage was applied to each axis separately, which was done through the use of a National Instruments Data Acquisition Card (NI DAQ PCI-6259). When the input to the scanning mirrors was set to zero volts, they act as a mirror which reflects the beam 90-degrees. The beam was then sent through two lenses with focal lengths of 100 mm and 150 mm, providing a magnification of 1.5x. They were separated from each other by the sum of the two focal lengths, or 250 mm, on an aluminum block. The aluminum block was free to move while keeping the distance between the two lenses fixed.

The purpose of the lenses was two-fold. First, they were aligned such that they directed the beam into the back of the objective regardless of the tilt angle produced by the scanning

mirrors. There were two ways that the alignment of this was done. First, the position of the objective was fixed and the distance between the first lens and the scanning mirrors could be adjusted. To make sure that proper alignment was achieved, the laser power was measured at the position of the back of the objective with the galvo mirrors set to zero tilt on both x and y. The galvo mirrors were then set such that the beam propagated at a different angle. The lenses were positioned by moving the aluminum block until the power is optimized. Alternatively, if the distance, d_1 between the scanning mirrors and the first lens were known, then for focal lengths f_1, f_2, and magnificaton $M=f_2/f_1$ the distance from the back of the second mirror to the objective, d_2, could be calculated using

$$d_2 = f_2 + M(f_2 - Md_1) \tag{2.7}$$

At this position, the beam reached the back of the objective at the same place regardless of the tilt angle that may have been set by the scanning mirrors. Again, to ensure proper alignment, the laser power was measured at the location of the back of the objective with the galvo mirrors set to some position other than zero in x and y. Finally, the position of the objective would be changed until the power was optimized. Practically, I found that the first alignment procedure worked much better than the second. To scan the sample, a voltage would be applied to either the x or y axis of the scanning mirrors. As mentioned above, this changed the tilt angle of the mirrors, which in turn changed the beam angle. Consequently, the beam would reach the back of the objective at a slightly different angle, and this would adjust the position of the spot at the front of the objective. By changing the tilt angle of the excitation beam using the scanning mirrors, the position of the focused beam could be moved while the sample remains stationary.

The sample was held in a similar configuration as it was before. A square breadboard was used in place of the rectangular one, and the objective was mounted to a one-axis piezosystem (Piezosystem Jena MIPOS 100) that allowed the objective to translate vertically a total of 100 μm. This was used for fine focusing of the objective. A large block of aluminum with holes tapped for 1/4-20 screws was affixed to the top of the breadboard to provide stabilization and for mounting the sample. The sample itself sat in an aluminum sample holder which was fixed to the aluminum block and could move manually along one axis. Since the beam wass adjusted in this configuration, it was not necessary for the sample to be mobile.

When a portion of the sample hits the beam and fluoresces, the light travels along on the same path. Just as before, instead of reflecting off the dichroic mirror the majority of

fluorescence passed through it and entered the final portion of the set up. In this configuration all of the back scattered light was sent to a single Fiber Port Collimators. After focusing the beam into a single mode fiber, the beam was split using a single-mode fiber splitter (FiberWDM - Visible wavelength division multiplexers). This replaced the 45:55 pellicle beamsplitter that was used in the previous version of the setup. The signal was measured using the same Perkin Elmer APDs from before.

All of the equipment in these experiments was controlled from a desktop computer using National Instruments LabVIEW software.

2.2.1 Initial Confocal Microscopy Measurements

In order to begin to test the confocal setup, it was necessary to use a calibration sample rather than just trying to look for NV centers in bulk diamond or in nanodiamonds, since after the initial alignment it was likely that things would need to be fine-tuned in order to optimize performance. To this end, a coverslip with gold patterns deposited onto it was used as a standard for optimizing performance. Although gold does not fluoresce in the bandwidth of the microscope when excited with 532 nm light, it is highly reflective and the amount of extra reflected light is more than enough to be detected above the noise floor of the images.

The standard glass slide had two different sizes of structures. The larger ones are shaped like either a "C" or an "L". The smaller ones on the other hand are designed as unique markers. In this way, they could be used to locate an NV center in a nanodiamond that had been found previously, or for repositioning the slide in the case of drift during the course of an experiment.

In general, I found it useful to use these gold markers as a first step in not only measuring images, but also doing fine adjustments to the detectors. As I mentioned above, the alignment procedure used involved overlapping the 532 nm beam and the 630 nm beams over long distances of the optics table. Even after all this was done, I initially found that when I went to measure images I could improve the amount of light that was collected by making slight adjustments to the mirrors that directed the beam into the Fiber Ports. What worked best was to first go to one of the large gold markers and then adjust until the counts were as high as possible. Then, move to one of the smaller markers and further optimize on those. Using only modest laser power (< 50 mW) it was possible to get $\sim 10^5$ counts per second (CPS) on the APDs.

After performing this optimization, the next step was to measure and identify single NV centers in nanodiamonds. At the beginning, two different avenues were pursued for preparing nanodiamond samples. The first was dropcasting a commercial solution onto a 25 x 25 mm glass coverslip (Corning® 25x25mm Square #1½ Cover Glass Product #2870-25). The other approach involved spin-coating at several hundred RMPs onto a glass coverslip, similar to procedures that are done to prepare quantum dots. Initially, I was unable to find NV centers at all in my confocal images on the spin-coated samples. The undiluted dropcast, on the other hand, often showed a few bright spots, but the counts on these spots were quite high, and other methods for determining if these were single NV centers (which I will describe later) all suggested that the emission was not coming from single emitters. At the time it seemed as though there was some form of aggregation of NV centers so that there were between > 5 NV centers in a cluster. However, it seemed statistically unlikely that this would keep happening. Methods such as sonication were pursued to try to reduce the amount of aggregation, but these did not appear to be successful. Another issue was that the when the sample was dropcast onto the slide, it would not spread uniformly over the coverslip.

In order to resolve these issues, a new procedure was developed for preparing nanodiamond samples. First, the commercial solution was diluted 100:1, as it was noticed that looking at a smaller region of a confocal image also showed discernible spots that were dimmer than the ones in the large scans. Additionally, it was necessary to clean the cover glass using soapy water, then drying it with air from the hood, and finally, cleaning the slide with ozone for ~10 minutes. This was done by placing the cover glass into a machine that ionized the air using UV light. The ionized air generated ozone, which would react with the surface of the glass and leave a cleanly terminated surface. Once all of these steps had been completed, nice nanodiamond samples were routinely prepared by dropcasting the diluted nanodiamond solution onto the clean cover glass. Representative images of the dropcast films before and after dilution are shown in figure 2.4. Using the bright NV Centers in the confocal images, it was possible to further optimize the system. When the system was well optimized, bright single NV centers in nanodiamonds produced count rates of approximately $\sim 2 \times 10^4$.

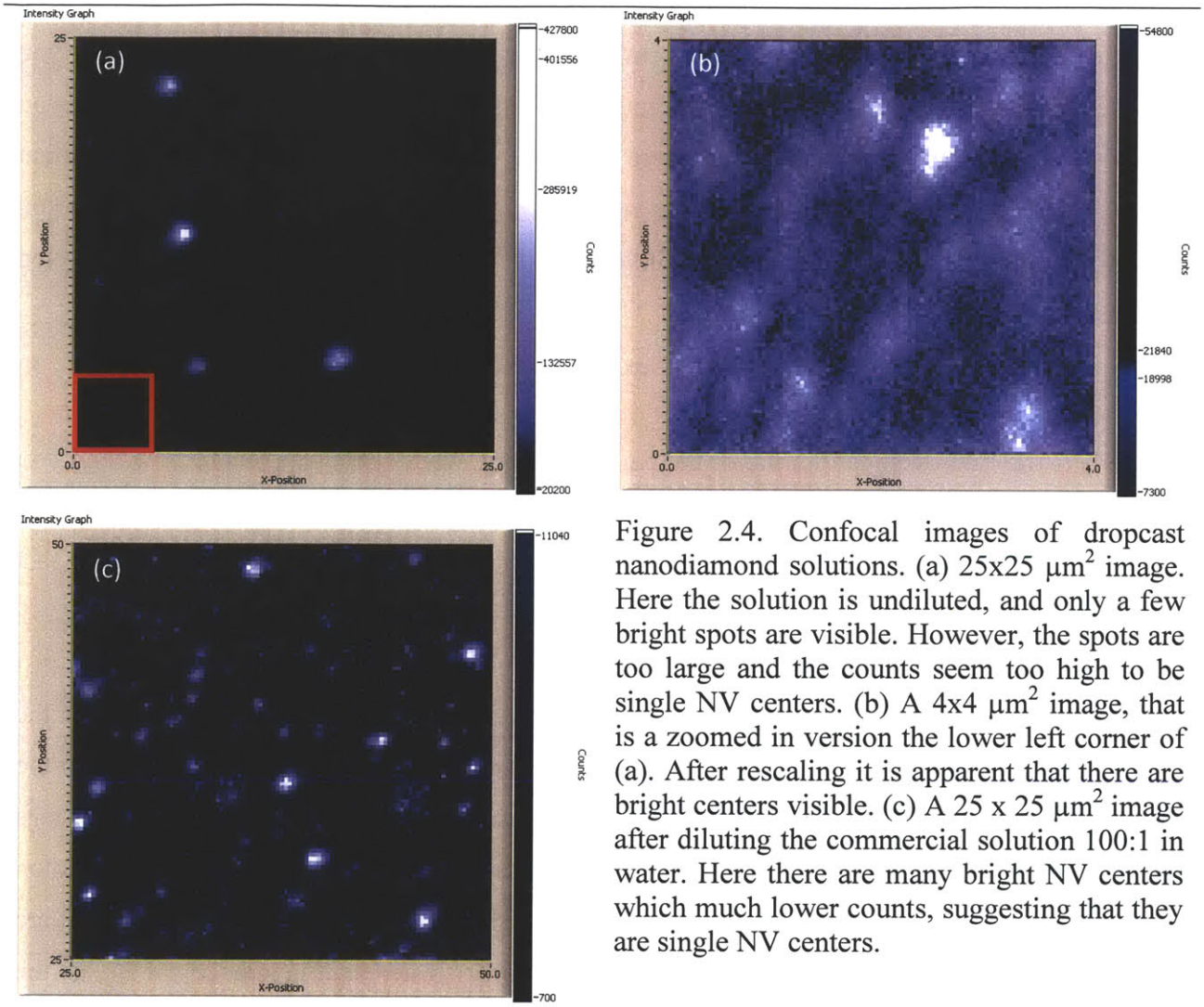

Figure 2.4. Confocal images of dropcast nanodiamond solutions. (a) 25x25 μm^2 image. Here the solution is undiluted, and only a few bright spots are visible. However, the spots are too large and the counts seem too high to be single NV centers. (b) A 4x4 μm^2 image, that is a zoomed in version the lower left corner of (a). After rescaling it is apparent that there are bright centers visible. (c) A 25 x 25 μm^2 image after diluting the commercial solution 100:1 in water. Here there are many bright NV centers which much lower counts, suggesting that they are single NV centers.

2.2.2 Single Emitter Determination

After being able to find bright spots in the confocal images, these spots had to be identified as NV centers. The search began by first identifying if the light that was being detected came as the emission from some kind of emitter or if it was just a reflection off of some dirt. This was done by measuring an antibunching trace [Kurtsiefer2000, Beveratos2001, Brouri2000].

Antibunching is a phenomenon of single emitters which have a finite emission lifetime. The way that it can be thought of is as follows: When you first excite an NV center, it absorbs the light and goes into some excited state. It then lives in that state for some time and later fluoresces and relaxes to its ground state. Only after this process can it absorb another photon

and later fluoresce. Consequently, if you were to watch the photon stream that comes back from a single emitter and look at the number of emission events spaced apart by some interval τ, you would find that you never get emission events that are spaced apart by $\tau = 0$. However, if you waited until $\tau = 1$ ns, you would see that there are some very small number of photon events that are spaced apart by that amount of time. As you get to larger and larger τ, the number of photon events that are spaced apart by increases. In general the amount of signal, $g(\tau)$, that is detected goes as

$$g(\tau) \propto 1 - \exp(-\tau / t_{fl}) \tag{2.8}$$

where t_{fl} is the fluorescence lifetime of the emitter. After a while it doesn't matter how long you wait, and the number of photon events is always the same. This can be converted to a probability by normalizing to the long time behavior, and it is very intuitive to think of it this way. The fact that the probability goes to zero is the phenomenon of "antibunching."

Measuring an antibunching trace is the same thing as making the measurement that I just described. Since the APDs are sensitive to single-photon events, these were used to register the time of the photon arrivals. The NI DAQ card is too slow to time the photon events, and so the PicoHarp (PicoQuant PicoHarp 300) was used to make this measurement. The Pico-Harp tags the time difference between successive photon events and is capable of tagging single photon events on the picoseconds timescale. It then builds a histogram of the number of events that are separated by certain time intervals. This time resolution is faster than is needed for us, as the fluorescence lifetime of the NV center is ~10 ns [Collins1983]. The signature of a single emitter is its response at $\tau = 0$ should be zero. If the emitter is a single emitter, then the probability of there being events spaced apart by $\tau = 0$ be zero. If there are two emitters, then it is possible that you could have two emission events spaced apart by $\tau = 0$, however, it is half as likely as having photon events spaced apart by much longer times. Consequently if you have two emitters then $g(\tau = 0) = 0.5$. In general, the $\tau = 0$ behavior for n emitters is given as

$$g_n(\tau = 0) = \frac{n-1}{n} \tag{2.9}$$

Several examples of antibunching traces are shown in figure 2.5. It is worth nothing that because of the background reflection and the fact that there is some noise to the APDs, the signal

at $\tau = 0$ is not exactly zero. Instead, it is sufficient to notice that for single emitters the signal is $<< 0.5$ at $\tau = 0$. In this regime the NV center follows sub-Poissonian statistics because the probability of detecting photon events is less than 1.

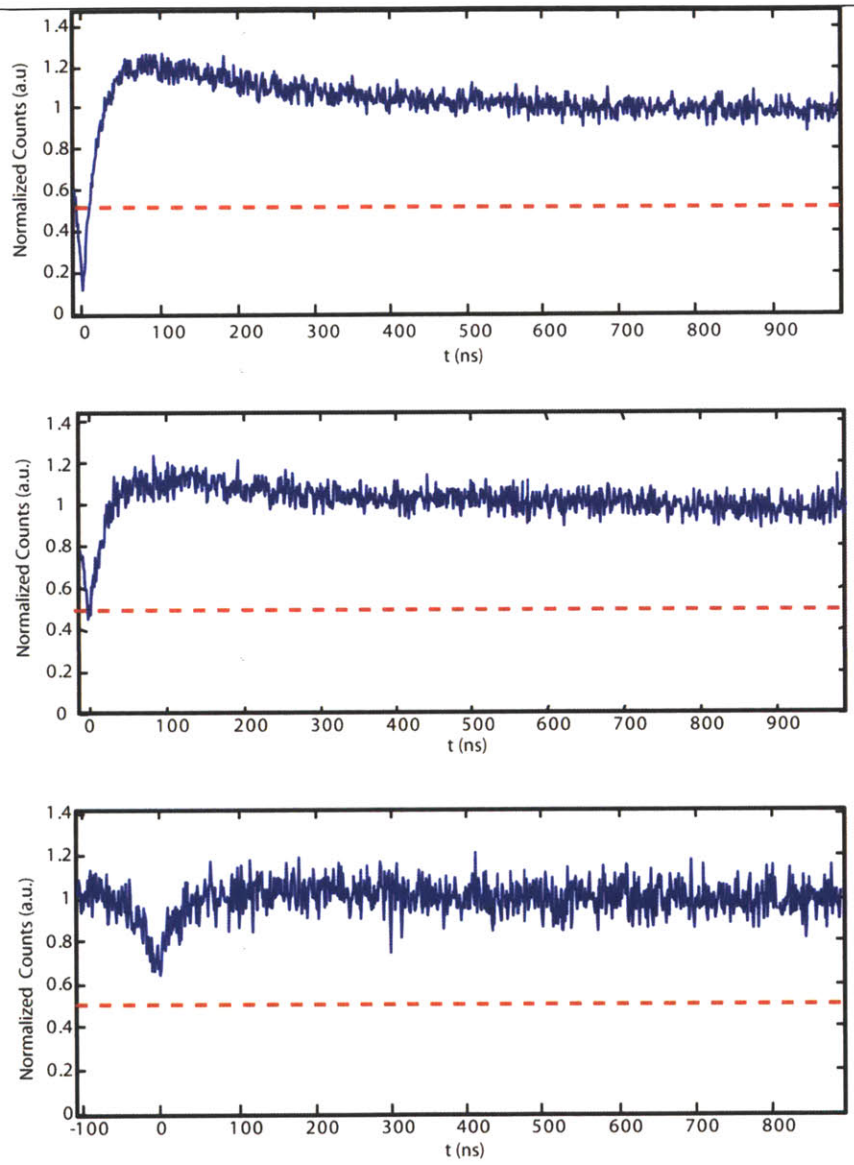

Figure 2.5. Antibunching traces. The number of NV centers at each spot increases from top to bottom, as evidenced by the increase in the dip relative to the dashed line at 0.5. The top trace drops well below, indicating a single emitter, the middle trace is at approximately 0.5, while the bottom trace is clearly above it, indicating more than 2 emitters.

While the antibunching traces of the NV center show the typical $\tau = 0$ and long time behavior, the behavior right after $\tau = 0$ is quite different. Indeed, when normalized the behavior after around 50 ns exceeds unity and the NV center is following super-Poissionian statistics. This behavior is known as "bunching" and intuitively what it means is that the NV center is more likely to emit at slightly longer times than its fluorescence lifetime than in the long-time limit.

The reason for this is because there are two mechanisms by which the NV center can relax to ground state. One of them, the faster one, is by fluorescence and is radiative, meaning that it leads to the emission of a photon. The other pathway is non-radiative, and does not lead to the emission of a photon. For each time the NV center is excited, in the short time limit any relaxation that happens is almost guaranteed to be happening because of fluorescence since the fluorescence pathway is much faster (10s of nanoseconds versus microseconds). In the longer time limit the NV center has two options – either emit a photon or not. This means that the number of photons emitted after 1 μs is going to be *less* than the number of photon events that are emitted with in the first 15 ns. A example showing a clear example of this behavior is shown in figure 2.6.

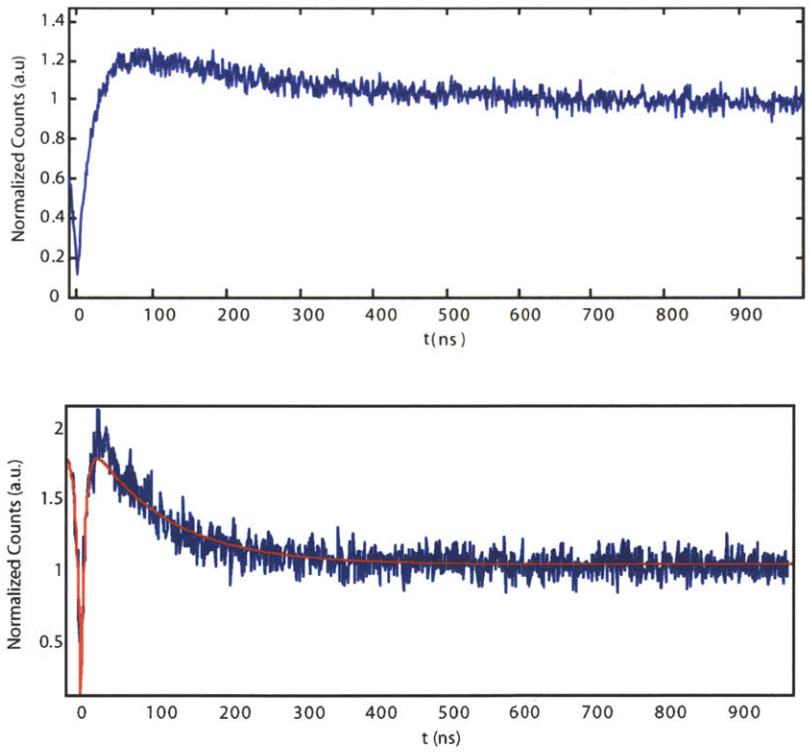

Figure 2.6. Antibuncing traces. (top) This trace shows clear sub-Poissionian statics at t = 0 which indicates that the signals are coming from a single emitter. (bottom) This trace shows strong super-Poissionian statistics right after t = 0.

2.2.3 Continuous Wave Microwave Experiments

The previous measurements were used to identify fluorescent single emitters that were likely single NV centers. While these experiments were sufficient to see that, measuring the spin properties of the emitter was necessary to confirm that the signal was coming from an NV center.

This was accomplished by measuring the Optically Detected Magnetic Resonance spectrum, or ODMR spectrum, of the NV center [Loubser1978, Balasubramanian2008].

Before describing the microwave experiments on the NV center, it is worth it to first examine its spin Hamiltonian. Although there are many terms, the relevant ones for this analysis written in reduced units are

$$\hat{H}_{NV} = D\hat{S}_z^2 + E(\hat{S}_x^2 - \hat{S}_y^2) + \gamma\vec{B}_z\hat{S}_z + \hat{S}\underline{\underline{A}}\hat{I} \tag{2.10}$$

The first term $D\hat{S}_z^2$ describes the zero-field, or crystal field, splitting of the NV center. This represents the splitting of the energies of the spin states in the absence of any field, electric or magnetic. The next them, $E(\hat{S}_x^2 - \hat{S}_y^2)$, is related to the energy splitting due to an electric field, which is also known as the Stark-Splitting. This field can be caused by either an external field [VanOort1990], or also caused by internal strain due to the lattice. The next term $\gamma\vec{B}_z\hat{S}_z$ represents the Zeeman-Splitting, which is the change in the energy levels due to an applied magnetic field. The final term is the hyperfine splitting. This includes information on how the energies of the spin states change in the presence of nearby paramagnetic nuclei, such as ^{13}C, ^{14}N, or ^{15}N.

As described in chapter 1, there are various electronic levels to the NV center. The spin states of ground and first excited states are both triplet states, meaning that the allowed values for $m_s = \{0,+1,-1\}$. Because the NV center is not spherically symmetric, it turns out that spin states are not all degenerate. The $m_s = 0$ lies lower in energy than the $m_s = +1$ or $m_s = -1$ levels. These two levels are degenerate, however, in the absence of an applied electric or magnetic field, and so using an microwave field that is tuned to the resonant frequency of the transition it is possible to drive a transition between the $m_s = 0$ and the $m_s = +1$ state, for example. While this might not appear to make any difference, it turns out that the NV center has different fluorescent rates depending on whether or not it is in the $m_s = 0$ state or not. The reason is because in the electronic excited state, the $m_s = +1$ or $m_s = -1$ states have increased probability of undergoing an intersystem crossing to a near-lying singlet state via spin-orbit coupling [Stoneham2001]. This singlet state does not relax via fluorescence, but rather non-radiatively. The $m_s = 0$ state also undergoes a similar non-radiative relaxation, but at a slower rate. Incidentally, it is this process

that causes a decrease in the photon count rate at long times which leads to the super-Poissionian statistics that are observed in the antibunching traces.

Measuring an ODMR trace begins by first locating a single emitter using the antibunching measurement described above. The next step was to sit on the single NV center and apply an AC magnetic field over the sample. When the frequency of the magnetic field matched the transition frequency, the spin state of the NV center would change from $m_s = 0$ to $m_s = \pm 1$. Measuring ODMR signals proved to be quite a challenging endeavor. The way that eventually worked for me was the following: a piece of cover glass with nanodiamonds on it was placed onto a piece of PCB board. This board had been custom designed such that a small (~ 25μm diameter) wire could be paid overtop of the cover glass. An AC current could then be passed through the wire, and this current in turn generates an AC magnetic field. Changing the frequency of the AC sources changes the frequency of the magnetic field, and so it was possible to tune the applied frequency. In the actual experiments, the current source was a Hittite Signal Generator (Hittite HMC-T2100) capable of generating signals with frequencies ranging from 10 MHz to 20 GHz. The output was amplified by a power amplifier (Minicircuits) and then connected to the PCB board using SMA connectors.

In order to detect signals that were induced by the presence of the magnetic field, the fields had to be gated in some controlled way. This was done through the use of a mixer and the output of the DAQ counter card. The DAQ card is capable of putting out a square wave signal at a well defined frequency and duty cycle. The mixer takes the input from the DAQ card and from the HMC-T2100 before amplification and multiplies them. When the voltage coming out of the DAQ card is low, the mixer does not pass any current through, and consequently there is no AC field at the sample. When the voltage coming out of the DAQ card is high, then current is passed through and there is an AC field at the sample. In these experiments, the frequency of the square wave from the DAQ card was set to 1 kHz and had a duty cycle of 0.5, meaning that for 500 μs there was no AC field at the sample and for 500 μs an AC field was present. The fluorescence was measured during these two different time periods and the ODMR signal was computed as

$$Signal = \frac{I_{w/\,AC\ field}}{I_{no\ AC\ field}}$$

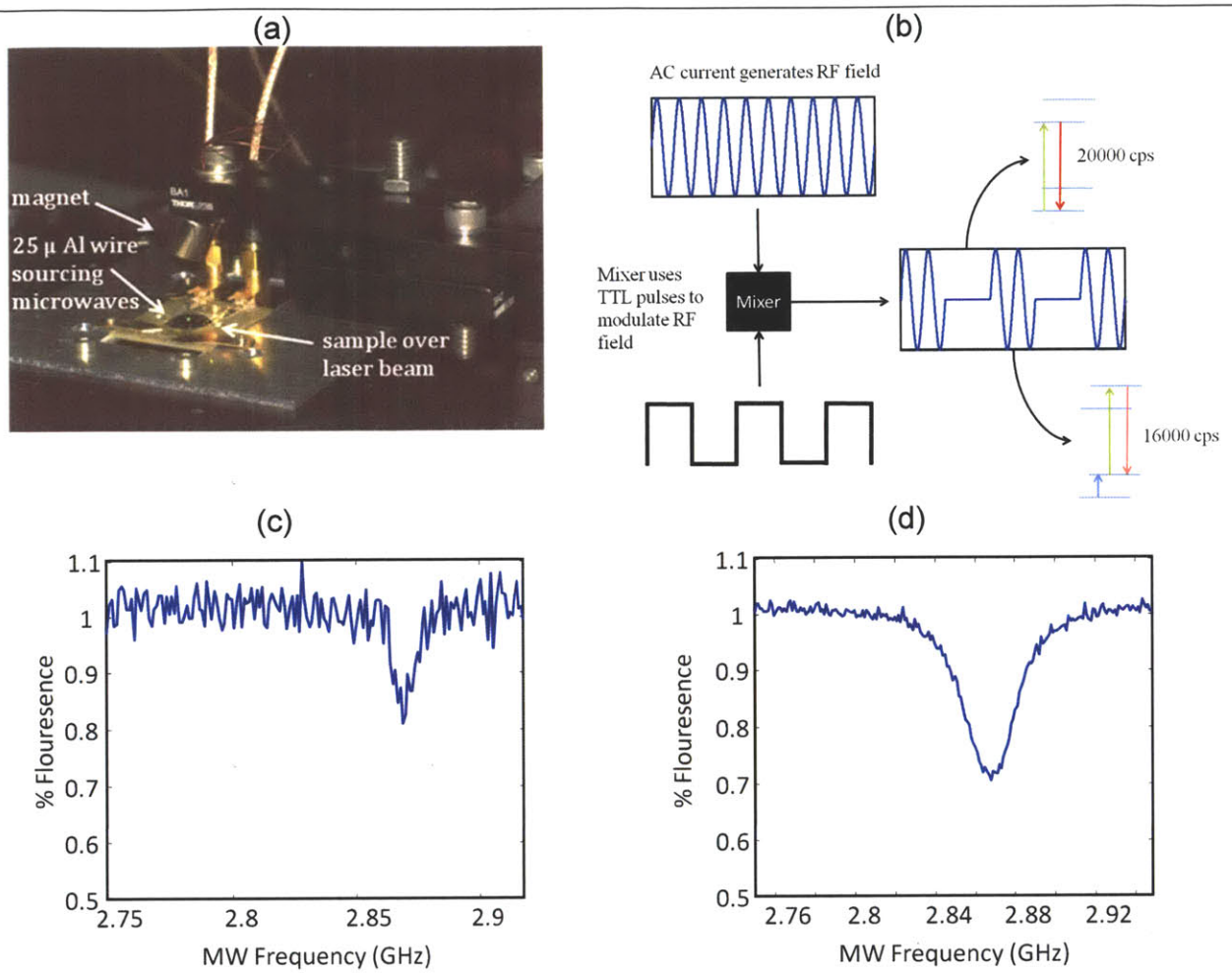

Figure 2.7. (a) Picture of experimental setup for measuring ODMR signals. The magnet above the sample is used to apply a static B-field to split the $m_s = +1$ and $m_s = -1$ states of the NV Center. (b) A schematic illustration of the way the electrical signals flow through the mixer and to the sample. The output is shown on the right. When there is an AC magnetic field tuned to the resonant frequency of the NV center, this causes a spin-flip transition which leads to a reduction in fluorescence. (c,d) Examples of ODMR traces taken with no static field applied. Here, (c) is an example of an ODMR trace of a single NV Center in bulk diamond while (d) is a trace taken of an NV in a nanodiamond. The reduction of noise in the nanodiamond case is due to the increased amount of fluorescence in the NV center.

Figure 2.7 shows images of the experimental setup as well as ODMR traces that were collected on single NV centers. For NV centers found in bulk diamond, a single signature dip in fluorescence occurred in the microwave, or RF, regime right at 2.87 GHz in excellent agreement with literature values [Balasubramanian2008]. In nanodiamonds this was almost never the case, and the ODMR spectra did not have just one resonance. Unlike bulk diamonds where the lattice is considerably large, nanodiamonds experience much larger strain due to their relatively small

size. This strain breaks the symmetry of the NV center and this splits the $m_s = +1$ and $m_s = -1$ lines. An alternate way of thinking of this is that the strain causes the electronic wavefunctions to become asymmetric, and this leads to an electric field developing around the NV center. This electric field then, through the Stark effect, splits the ODMR lines. In the example shown in figure 2.7, this splitting is not visible because of the high power of the RF field because of power broadening. As shown in figure 2.8, reducing the microwave power leads to a narrowing of the ODMR lines and with sufficiently low-power the individual ODMR lines can be resolved.

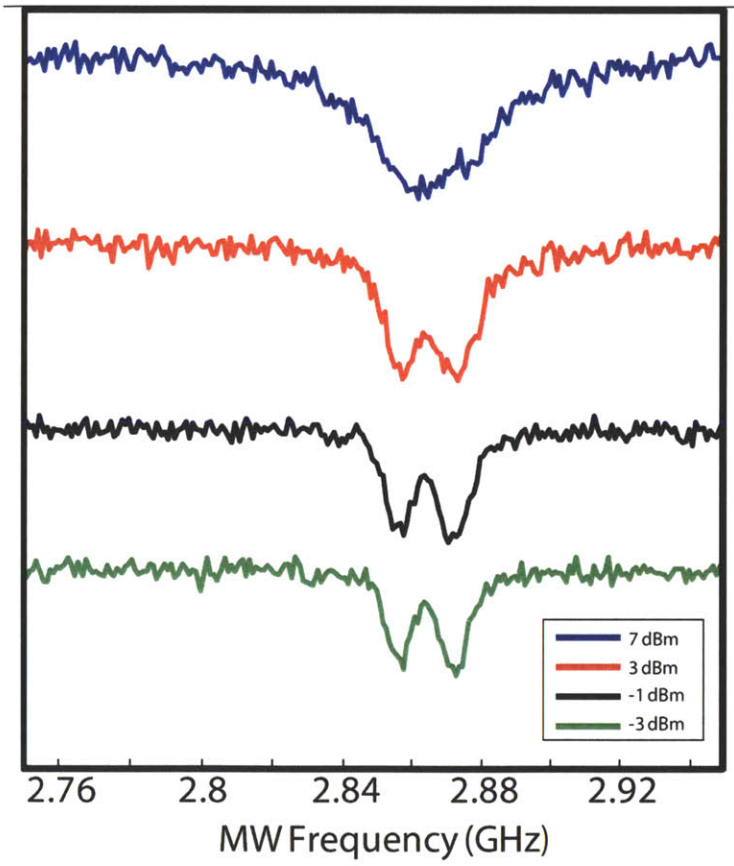

Figure 2.8. Traces showing the narrowing of the ODMR lines in an NV in a nanodiamond as a function of microwave power. The unit of power is dBm, which represents the power of the current prior to being amplified. At near the maximum value of 7 dBm, the individual lines in the trace are too broad to be resolved, even with such a large splitting. As the power is decreased, the splitting becomes apparent.

Strain is one mechanism by which the ODMR lines in the NV center can be split. The other mechanisms include the Zeeman-effect and hyperfine coupling. In the case of the Zeeman-effect, a static B-field (nominally alingned along the NV axis) couples to the NV-dipole moment. Thinking classically, the NV dipole is a magnetic dipole and so it wants to align itself to the applied magnetic field. The three spin states, $m_s = +1$, 0, and -1 correspond to the dipole being oriented directly along, perpendicular to, and directly against, the NV axis. Consequently, the

energy of the +1 spin state would increase and that of the -1 state would decreas in energy, while the zero state remains unchanged. This leads to a reduction in the frequency for the $m_s = 0 \rightarrow -1$ transition and in an increase in the frequency for the $m_s = 0 \rightarrow +1$ transition. The magnitude of the change depends on the strength of the applied field and is scaled by the constant, $\gamma = 2.8$ MHz/Gauss. Examples are shown in figure 2.9.

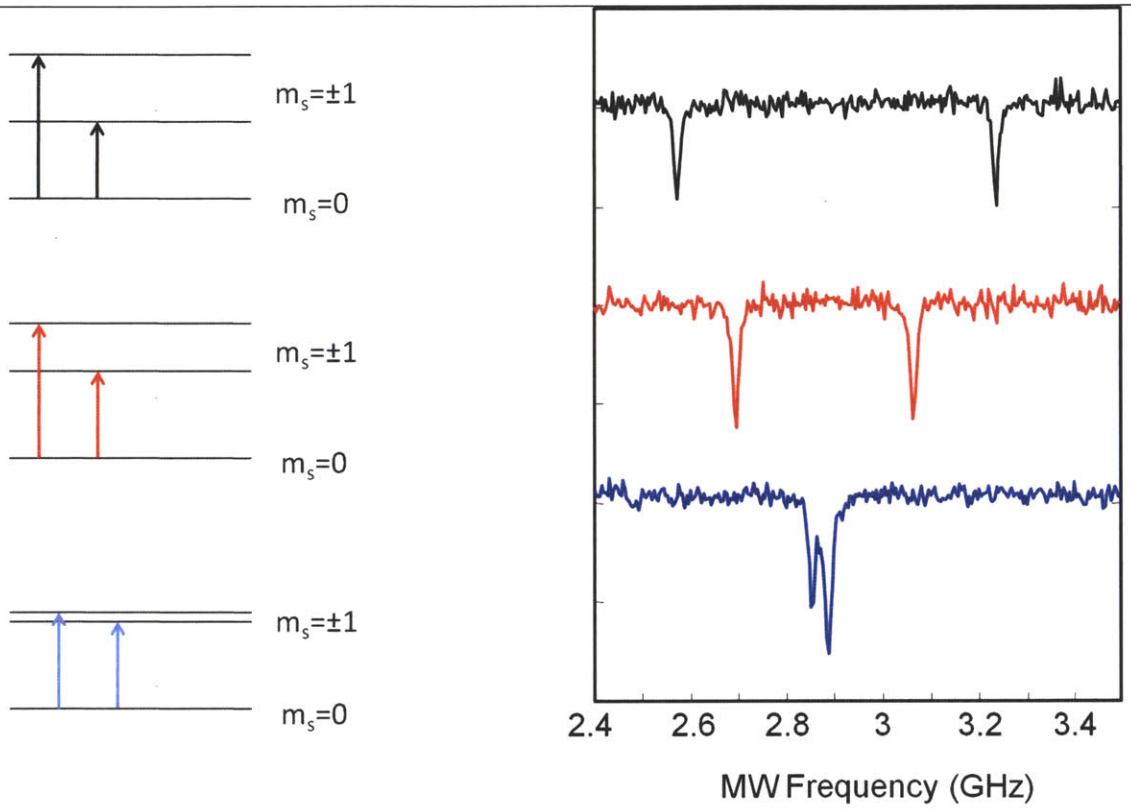

Figure 2.9. ODMR traces of NV centers in nanodiamonds with various B-fields. As the applied field gets stronger and stronger, the splitting between the $m_s = +1$ and $m_s = -1$ lines increases. This also manifests itself in the separation between the transitions in the ODMR traces themselves. At zero field (blue trace) the splitting is due to strain in the nanodimaond.

The last mechanism for splitting the ODMR lines that I will discuss is hyperfine coupling. Hyperfine coupling is caused by nearby paramagnetic nuclei. Again, thinking classically, these nearby nuclei produce a local magnetic field which is felt by the NV center, and consequently changes the energy levels of the spin states. The amount of the change in the energy levels depends on the nuclei causing the change and the proximity from the NV center to that nucleus. In all cases for the NV center, since nitrogen is a paramagnetic nucleus there is always going to be a splitting of the ODMR lines because of it. The amount of the splitting and

the number of additional lines depends on whether or not this is caused by ^{15}N or ^{14}N. The number of additional lines for a nucleus with nuclear spin I is $2I+1$, or the spin-multiplicity of that nucleus. For ^{14}N, which has I = 1, each ODMR line is split into a triplet with the spacing of ~2 MHz, while for ^{15}N, which has I = 1/2, the ODMR lines are split into doublets with a spacing of ~ 3MHz [He1993(1), He1993(2)]. This offers a unique ability to identify the type of nitrogen atom that is used to form the NV center. The other major nucleus of interest in this is ^{13}C, which also has I = 1/2. This also splits the signals into doubles, but by a much larger amount than ^{15}N. For ^{13}C that are directly in the NV center, the splitting is on the order of ~130 MHz and drops as the ^{13}C gets further and further from the NV site.

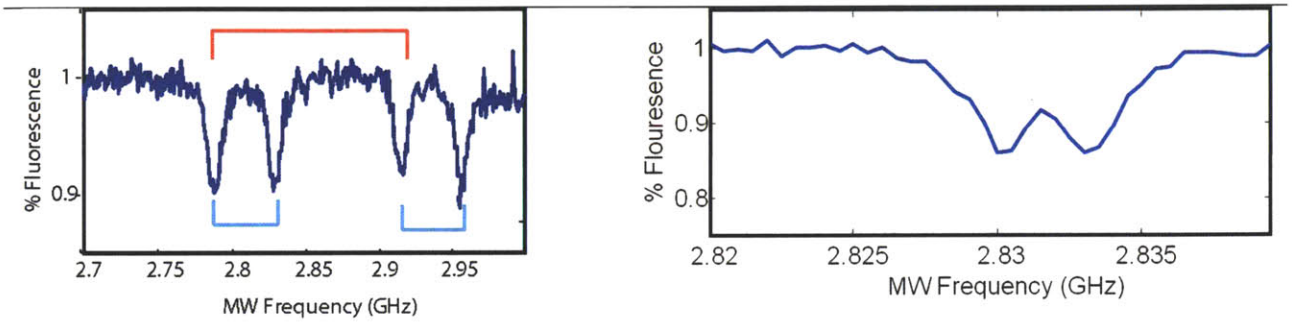

Figure 2.10. Examples of ODMR spectra which are split due to the hyperfine interaction. (left) The smaller splitting, indicated by the blue lines, is caused by an applied field, while the large splitting, indicated with the red lines, is caused by the presence of a ^{13}C in the NV center. (right) A much smaller splitting due to the ^{15}N in the NV center.

2.2.4 Pulsed Microwave Experiments

The last set of experiments that I performed were pulsed microwave, or RF experiments. Unlike the previous measurements that I made, the pulsed RF experiments all focused on studying to coherence properties of the NV center. They involved preparing and measuring how populations and coherences interact with each other and with their perturbing environment. [Zhang2004, Windsor1998, Holmstrom1997, Manson1996].

The first of these experiments is the classic Rabi-cycling experiment. In this experiment, a coupling, V, is artificially introduced which couples two different eigenstates states of the zero-order Hamiltonian, with energies E_0 and E_1. Effectively, this means that the Hamiltonian for the system can be written as $\hat{H} = \hat{H}_0 + \hat{V}$. In the limit of large coupling (ie. when V ~ $|E_1 - E_0|$) it is no longer reasonable to think of these two states as eigenstates anymore, and the true eigenstates

of the system become some mixture of the two. However, once the coupling turns off, the system can adequately be described by the initial eigenstates.

It is much easier to develop an intuition for what is going on by first going through the math and then analyzing the results [Bernath2005, Griffiths2005]. Here, we have two eigenstates which in the case of the NV center are the $m_s = 0$ and $m_s = 1$ states. In this case, the energies of the $m_s = +1$ and $m_s = -1$ states have been split by a DC magnetic field so that it is possible to address only one transition. These states have energy E_0 and E_1 along with corresponding frequencies ω_0 and ω_1. Initially, the state of the NV center is given by a superposition of these two states

$$|\Psi\rangle = a_0(t)|0\rangle e^{-i\omega_0 t} + a_1(t)|1\rangle e^{-i\omega_1 t} \tag{2.11}$$

In the absence of the coupling, the coefficients in this problem would be time-independent since the states $|0\rangle$ and $|1\rangle$ are eigenstates of the original Hamiltonian. This superposition is required to satisfy the Time-Dependent Schrodinger Equation.

$$H|\Psi\rangle = i\hbar\frac{\partial}{\partial t}|\Psi\rangle \tag{2.12}$$

Multiplying both the left hand side and right hand side of equation 2.12 by $\langle\Psi|$, the time evolution of the coefficients can be shown to satisfy the following coupled differential equations

$$i\hbar\dot{a}_0 = a_0\langle 0|V|0\rangle + a_1\langle 0|V|1\rangle e^{-i\omega_{10}t} \tag{2.13a}$$
$$i\hbar\dot{a}_1 = a_1\langle 1|V|1\rangle + a_0\langle 1|V|0\rangle e^{i\omega_{10}t} \tag{2.13b}$$

where $\omega_{10} = \omega_1 - \omega_0$. In the case of the NV center, the coupling is caused by an *off-axis* magnetic field interacting with the NV dipole moment, μ_{NV}. Hence, we can write

$$V = -\hat{\mu}_{NV}B\cos(\omega t) = -\frac{1}{2}\hat{\mu}_{NV}B\left(e^{-i\omega t} + e^{i\omega t}\right) \tag{2.14}$$

The important thing to know about the dipole operator in this case is that $\langle i|\mu|j\rangle = 0$ when $i \neq j$ and otherwise the product can be written as M_{ij}. This quantity is known as the transition dipole moment. Continuing along, the equations for the coefficients can be written as

$$\dot{a}_0 = i\frac{1}{2}a_1\omega_R\left(e^{i(\omega-\omega_{10})t} + e^{-i(\omega+\omega_{10})t}\right) \tag{2.15a}$$

$$\dot{a}_1 = i\frac{1}{2}a_0\omega_R\left(e^{-i(\omega-\omega_{10})t} + e^{i(\omega+\omega_{10})t}\right) \tag{2.15b}$$

where $\omega_R = \frac{M_{01}B}{\hbar}$ is the Rabi frequency. In order to solve this, we first invoke the rotating-wave approximation which allows us to throw away terms that contain $\omega+\omega_{10}$ in the exponent. The physical reason for this is because these represent waves that are oscillating too quickly to drive the transition efficiently. By doing this and defining the detuning frequency, $\Delta = \omega-\omega_{10}$, the equations can be solved by plugging the derivative of the first into the second one. Rather than going through all the details here, I present the result of solving the above two equations

$$a_0 = \left(\cos\left(\frac{\sqrt{\omega_R^2+\Delta^2}}{2}t\right) - i\frac{\Delta}{\sqrt{\omega_R^2+\Delta^2}}\sin\left(\frac{\sqrt{\omega_R^2+\Delta^2}}{2}t\right)\right)e^{i\Delta t/2} \tag{2.16}$$

$$a_1 = i\frac{\omega_R}{\sqrt{\omega_R^2+\Delta^2}}\sin\left(\frac{\sqrt{\omega_R^2+\Delta^2}}{2}t\right)e^{-i\Delta t/2} \tag{2.17}$$

In order to get to this point, I assumed that initially all of the population was in the $m_s = 0$ state. The more interesting consideration here is the time dependent probabilities of these states, which is obtained by taking the square modulus of each of these terms. This gives

$$|a_0|^2 = 1 - \frac{\omega_R^2}{\omega_R^2+\Delta^2}\sin^2\left(\frac{\sqrt{\omega_R^2+\Delta^2}}{2}t\right) \tag{2.18a}$$

$$|a_1|^2 = \frac{\omega_R^2}{\omega_R^2+\Delta^2}\sin^2\left(\frac{\sqrt{\omega_R^2+\Delta^2}}{2}t\right) \tag{2.18b}$$

Looking at these results, we see that the states have a conveniently simple form. The populations in the states all oscillate with a frequency $\frac{\sqrt{\omega_R^2+\Delta^2}}{2}$. Depending on the value of Δ,

the amount of population that can be moved from one state to the other changes significantly. When Δ is very large, the coefficient in front of the sin term is very small, and so only a little population transfer can happen. When $\Delta = 0$, meaning that the applied field is directly on resonance, the solutions become

$$|a_0|^2 = \cos^2\left(\frac{\omega_R}{2}t\right) \tag{2.19a}$$

$$|a_1|^2 = \sin^2\left(\frac{\omega_R}{2}t\right) \tag{2.19b}$$

In this case, it is possible to do a full population transfer from one state to another as long as the field is applied for $t = \pi/\omega_R$. This is known as a π-pulse. If the field is turned off at that point, the state has all of the population in the $m_s = 1$ state. Should the field be applied for half that amount of time, known as a $\pi/2$ pulse, the system will be in a coherent superposition of these two states.

For the NV center, the relative populations in the $m_s = 0$ and $|m_s| = 1$ states can be determined by measuring the fluorescence after applying a B-field for a certain amount of time. This was accomplished by gating both the laser source as well as the microwave source. Both sources were controlled using a Spin-Core Pulseblaster card (SpinCore PulseBlaster ESR). The Pulseblaster has 4 output channels, which can output TTL pulses of various durations with a resolution of ~2 ns. One of the output channels was connected to the AOM, and was used to turn the AOM on for a duration of 1μs. During this time, the fluorescence was measured and the amount of fluorescence was recorded as a reference value. Following this, another channel output a signal that was connected to the same mixer that was used for the ODMR measurements. This made it possible to apply a RF field that was resonant with the NV transition for a controllable amount of time, τ. After that duration, the laser was fired again for 1μs and the fluorescence was collected again, this time storing the value as the signal. The final optical pulse also serves to reset the NV spin back into $m_s = 0$ state. This was only possible because the NV center is known to be spin-polarized when it is excited optically. [Harrison2004] This experiment was repeated approximately 10^5 times for a specific time delay, which was stepped. The change in fluorescence was measured as

$$\Delta I = \frac{I_{ref}}{I_{sig}} \tag{2.20}$$

and plotted as a function of delay time, τ. The pulse sequence and an example of a typical rabi trace is shown in figure 2.11.

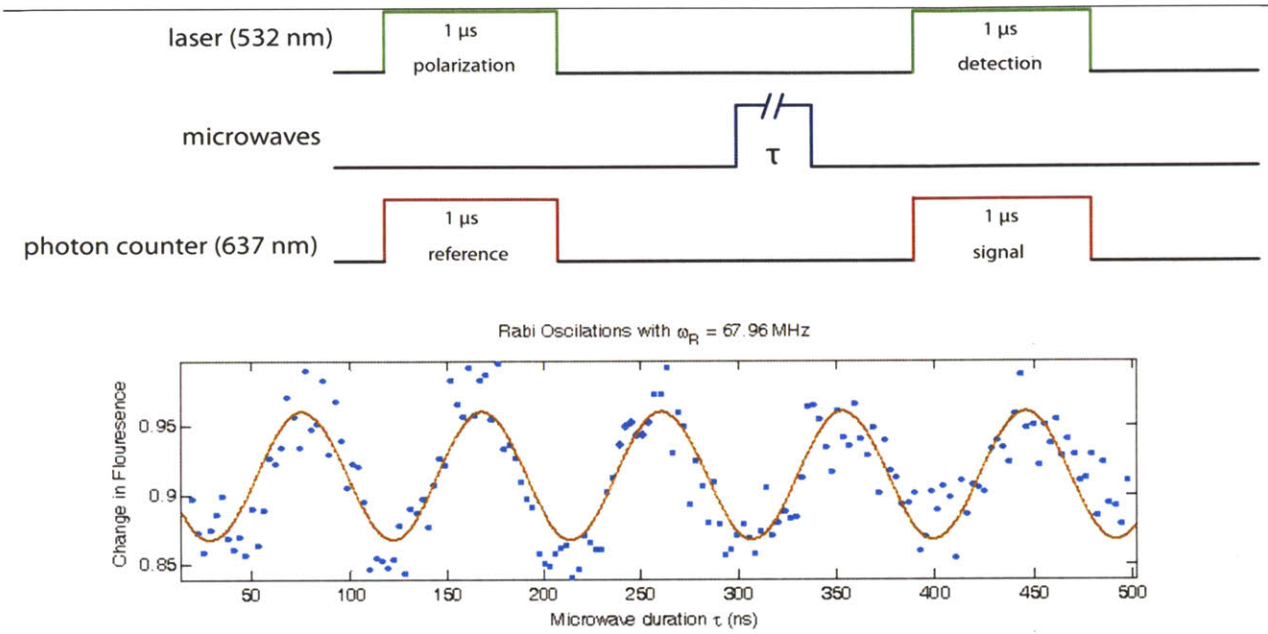

Figure 2.11. (top) Pulse sequence for Rabi-Cycling experiment. The laser pulse is fired before and after the measurement to collect the reference and signal traces, as well as to reset the NV center back to the zero state. The microwave field is applied in between for a variable number of nanoseconds. (bottom). An example of a Rabi-cycling trace, clearly showing oscillations in fluorescence.

The rabi-cycling experiment shows the ability to coherently control the NV center. For example, as I mentioned above it is possible to put the NV spin into a coherent superposition of two different spin states. Using various different pulse sequences that have been developed in the NMR community, it is possible to use the NV center to learn about its local environment. One of the simplest ways to do this is through a spin echo experiment.

The NV spin echo experiment is a slightly modified version of the Hahn Echo experiment that is commonly used in the NMR community [Hahn1950]. When doing this experiment on NV centers, a similar microwave pulse sequence is used in order to measure the coherence time, T_2, of the NV spin. One of the most intuitive ways to think about what is going during these pulse sequences is to picture the entire thing along the "Bloch Sphere." [NielsonChuang2004] Mathematically, it is a sphere that is centered at the origin with a radius of 1. The north and south poles of the sphere correspond to the states $|0\rangle$ and $|1\rangle$, respectively. The points on the surface

of the sphere correspond to different coherent superpositions. For example, the quantum state $|0\rangle$ would be represented on the bloch sphere as the vector (0,0,1). The quantum state $|1\rangle$ would be represented as (0,0,-1). The coherent superposition $\sqrt{\frac{1}{2}}(|0\rangle+|1\rangle)$ would represented as (1,0,0), while the coherent superposition $\sqrt{\frac{1}{2}}(|0\rangle+i|1\rangle)$ is represented by the vector (0,1,0). In general, any superposition state $|\psi\rangle$ can be written down applying the angles shown in figure 2.12 to the following formula

$$|\psi\rangle=\cos\left(\frac{\theta}{2}\right)|0\rangle+(\cos(\phi)+i\sin(\phi))\sin\left(\frac{\theta}{2}\right)|1\rangle \tag{2.21}$$

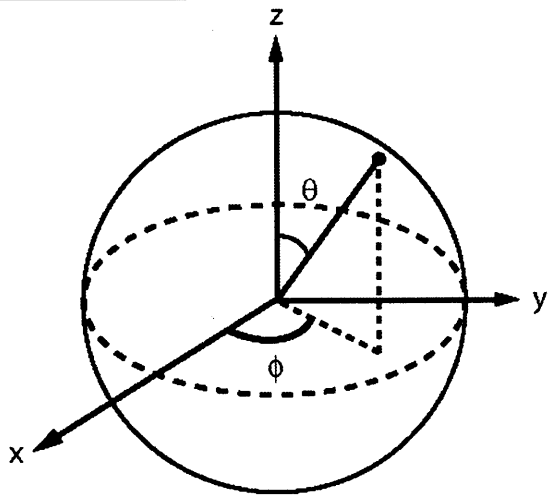

Figure 2.12. Visualization of the Bloch sphere. Any coherent superposition of a two-level system can be represented as a point on the surface of the sphere through equation 2.21 and the angles on the figure.

The spin-echo pulse sequence begins with a $\pi/2$ pulse, which puts the system into a coherent superposition. After this time, the field is turned off, and the NV spin is allowed to evolve under the field-free conditions for a time τ. During this time the states $|0\rangle$ and $|1\rangle$ acquire absolute phases at rates that are proportional to their natural oscillation frequencies, ω_0 and ω_1, respectively. It is important to note that ω_1 depends on the strength of the field applied, since $\omega_1=\frac{E_1}{\hbar}=\frac{\gamma B}{\hbar}$. In reality, the only thing that matters is the relative phase between the two states, so it is common to just talk about the phase of $|1\rangle$ relative to $|0\rangle$. Hence, the relative phase

between states $|0\rangle$ and $|1\rangle$ is $\omega_{10}\tau$, where $\omega_{10} = \omega_1 - \omega_0$. After this time duration, a π-pulse is applied which causes a population inversion and effectively moves the phase from the $|1\rangle$ state to the $|0\rangle$ state. During a second waiting time, τ', the $|1\rangle$ state again acquires a relative phase $\omega_{10}\tau'$ relative to the $|0\rangle$ state. At the end, unlike with the standard Hahn-Echo sequence, a final $\pi/2$ pulse converts the coherences back into populations, and these can be measured via fluorescence. The pulse sequence and bloch-sphere representation can be found in figure 2.13. If the amount of phase acquired between the two wait times are identical, the final $\pi/2$ pulse returns the NV spin back to the $|0\rangle$, yielding a large amount of fluorescence. If the amount of phase acquired is different, the last pulse moves the system into a different superposition which has an equal probability of emitting from either the $|0\rangle$ or the $|1\rangle$ state, and this yields less fluorescence.

(a)

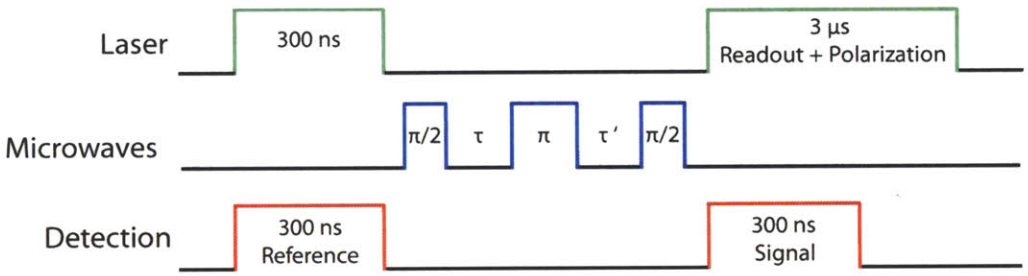

(b)

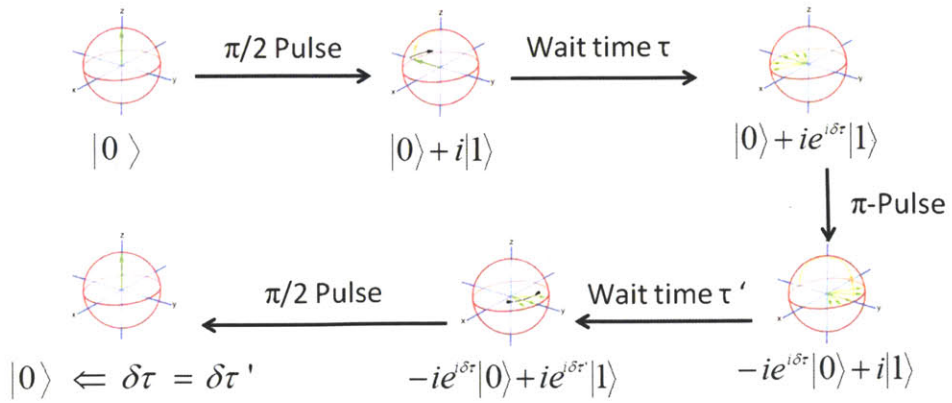

Figure 2.13. (a) Pulse sequence of Spin echo experiments. As with the rabi cycling experiment, the readout for the NV spin was via fluorescence. (b) Bloch Sphere representation of the evolution of the NV spin during the Spin Echo sequence. Images are adapted from [Filler].

There are two ways that the spin-echo experiment can be performed, and the two different measurements yield different results. The first is to fix τ and vary τ'. In this case, the only time that the phases are the same is when $\tau = \tau$'. At this point, there is a peak in the fluorescence. This same measurement can be made for various different values of τ, and the same trend occurs. Examples are shown in figure 2.14.

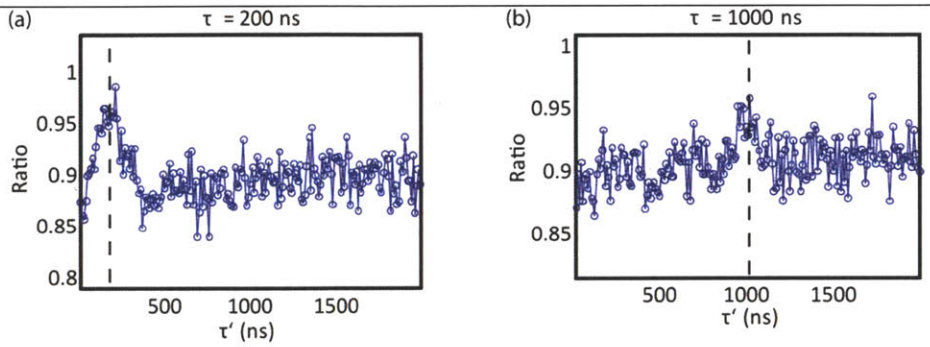

Figure 2.14. Examples of spin echo traces where τ was fixed and τ' was varied. It can be seen in both (a) and (b) that when the times are off, there is no revival. In (b) it is also noticeable that there is a decrease in the strength of the signal even at the echo revival. This is due to the rapidly fluctuating ^{13}C present in the diamond lattice.

The other way that the experiment can be done is to vary both τ and τ' in unison and measure the fluorescence. This ensures that you effectively sit at the top of the echo and always measure the maximum amount of fluorescence. An example of this kind of measurement is shown in figure 2.15. This measurement is analogous to measuring T_2 in NMR.

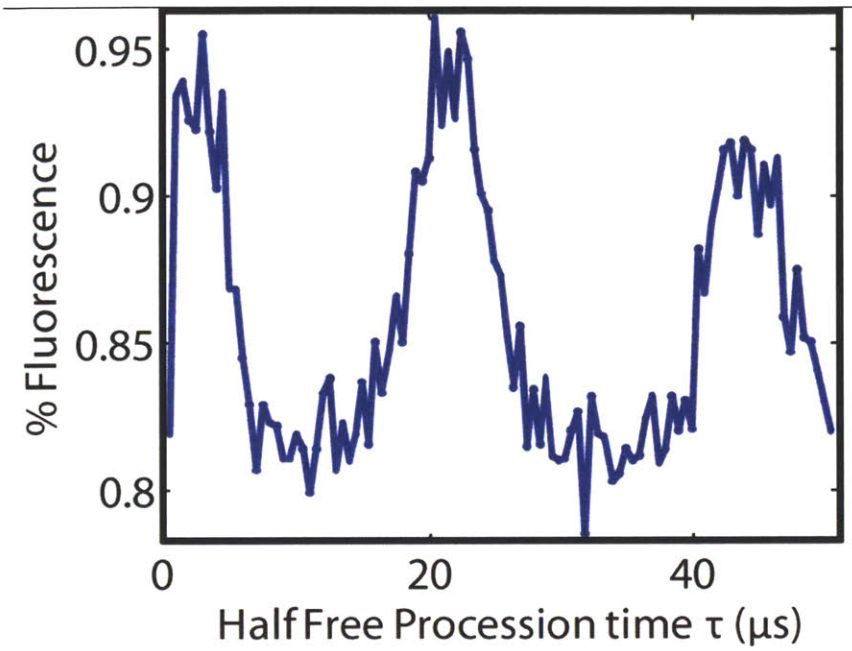

Figure 2.15. An example of a spin-echo trace showing echo-revivals. The revival time is inversely proportional to the strength of the applied B-field, and is scaled by the gyromagnetic ratio of the ^{13}C. Consequently, it can be used to accurately determine the B-field.

Looking at the NV measurement, there are clear and striking differences between the classic NMR case and the one of the NV center. Here, there is a decay which happens on the microsecond to 10s of microseconds timescale, but if one waits long enough there is a revival in the echo signal [Childress2006]. There are a few ways to think about this, but perhaps the most qualitative way is as follows: The bath that the NV center lives in consists of mostly diamagnetic nuclear spins – that is ^{12}C nuclei. However, 1% of the nuclei in the lattice are ^{13}C spins, which are paramagnetic. In the presence of an applied field, paramagnetic nuclei process at a rate known as their Larmor frequency, $\omega_L = \gamma_C B$, where B is the strength of the static field applied which also splits the $m_s = +1$ and -1 sates, and γ_C is the gyromagnetic ratio of the ^{13}C. Now as these spins process, they in turn are generating a periodic, time varying magnetic field, which is sensed by the NV spin. Since, as stated above, the free-procession frequency of the $|1\rangle$ spin state, ω_1, depends on the field strength, a time varying magnetic field will cause different amounts of phase to accumulate during the two wait times, τ and τ'. Hence, even when the two wait times are the same, the amount of phase acquired during those times is different and so the final $\pi/2$ pulse in the sequence does not return the NV back to the $|1\rangle$ state, but leaves it in a superposition. The reason that revivals are seen at all is because the time varying field that is generated by the nuclear spins is periodic. This means that if the waiting times τ and τ' are integer multiples of $1/\omega_L$, the effect of the time-varying field on the phase averages out, and the

final $\pi/2$ pulse resets the NV spin back into the $|0\rangle$ state. This can be verified by changing the static B-field. For larger fields, it is observed that the echo-revival time, t_{echo}, gets shorter. Further confirmation of this idea comes from plotting the |B| vs $1/t_{echo}$. Doing this yield a straight line relationship, with a slope of 1.071 kHz Gauss^{-1}, which precisely matches the Larmor frequency for ^{13}C.

Once the revival times have been accounted for, it is possible to determine T_2, the decoherence time for the NV center. By either mapping out the entire curve or just measuring at the revivals, the T_2 for the NV center can be obtained by fitting to the function, adapted from [Childress2006]

$$I(t) = A\exp\left[-\frac{(2t)^{n_1}}{T_2^3}\right] \times \sum_{k=0}^{N} \exp\left[-\frac{(t-k\tau_r)^{n_2}}{(2\tau_c)^2}\right] + C \tag{2.23}$$

In general I fit with the parameters $n_1 = 3$ and $n_2 = 2$ and would usually obtain T_2 values on the order of 150 μs for NVs in bulk diamond. Using NVs in nanodiamonds yielded much lower T_2 times, on the order of microseconds. This is consistent with work that had been done previously in bulk diamond [Jelezko2004, Childress2006], as well as on nanodiamonds [Tisler2009]. The main cause of the decoherence in the nanodiamonds comes from the interaction with the large number of nearby spins, leading to rapid decoherence. In the same work, it was shown that cleaning nanodiamonds to remove any residual surface spins increased T_2. In addition, generating NV centers in diamonds that have been artificially grown to significantly decrease the amount of ^{13}C has shown the ability to extend the T_2 to the order of milliseconds [Balasubramanian2009].

With this, I conclude the initial work that I did preparing and testing my microscope for doing experiments. The next chapter of my thesis focuses on work that I did on shallow implanted NV centers, and borrows heavily from the techniques that were developed in this chapter.

References:

[Balasubramanian2008] Balasubramanian, G., et al., "Nanoscale imaging magnetomtery with diamond spins under ambient conditions" Nature, 455 648 (2008)

[Balasubramanian2009] Balasubramanian, G. et al. "Ultralong Spin Coherence Time in Isotopically Engineered Diamond." Nat. Mater. 8, 383–387 (2009)

[Bernath2005] Bernath P., Spectra of Atoms and Molecules, Oxford University Press, New York, NY (2005)

[Beveratos2001] Beveratos, A., et al., "Nonclassical radiation from diamond nanocrystals", Phys. Rev. A 64(6), 061802 (2001).

[BornWolf1999] Max Born, Emil Wolf, Principles of Optics, Cambridge University Press, New York, NY (1999)

[Brouri2000] Brouri, R., et al., "Photon antibunching in the fluorescence of individual color centres in diamond", Opt. Lett. 25(17), 1294–1296 (2000).

[Childress2006] Childress, L., et al. "Coherent dynamics of coupled electron and nuclear spin qubits in diamond", Science 314, 281 (2006)

[Collins1983] Collins, A.T., et al., "Luminescence decay time of the 1.945 eV centre in type Ib diamond", J. Phys. C, Solid State Phys. 16(11), 2177–2181 (1983).

[Filler] Filler, A.G., "Spin Echo" article on www.wikipedia.com

[Glasbeek1991] Glasbeek, M., VanOort, E., "Coherent transients of the N–V centre in diamond", Radiat. Eff. Defects Solids 119, 301–306 (1991)

[Goodman2004] Goodman, J.W., Introduction to Fourier Optics, Roberts & Company Publishers, Greenwood Village, CO (2004)

[Griffiths2005] Griffiths, D., Introduction to Quantum Mechanics, Prentice Hall, Upper Saddle River, NJ (2005)

[Gruber1997] Gruber, A., Drabenstedt, A., et al., "Scanning Confocal Optical Microscopy and Magnetic Resonance on Single Defect Centers" Science 276(5321), 2012–2014 (1997).

[Hahn1950] E.L. Hahn, "Spin echoes". Physical Review 80: 580–594 (1950)

[Harrison2004] Harrison, J., et al., "Optical spin polarisation of the N–V centre in diamond", J. Lumin. 107(1–4), 245–248 (2004).

[Haus1984] Haus, H.A., Waves and Fields in Optoelectronics, Prentice Hall, Englewood Cliffs, NJ (1984)

[He1993(1)] He, X.F., et al., "Paramagnetic-resonance of photoexcited N–V defects in diamond, 1. level anticrossing in the (3)a ground-state", Phys. Rev. B 47(14), 8809–8815 (1993).

[He1993(2)] He, X.F., et al., "Paramagnetic-resonance of photoexcited N–V defects in diamond. 2. Hyperfine interaction with the N-14 nucleus", Phys. Rev. B 47(14), 8816–8822 (1993).

[Holmstrom1997] Holmstrom, S.A., et al., "Spin echo at the Rabi frequency in solids", Phys. Rev. Lett. 78(2), 302–305 (1997).

[Jelezko2004] Jelezko, F., et al. "Observation of Coherent Oscillations in a Single Electron Spin" Phys. Rev. Lett. 92, 76401 (2004)

[Kurtsiefer2000] Kurtsiefer, C., et al., "Stable solid-state source of single photons", Phys. Rev. Lett. 85(2), 290–293 (2000).

[Loubser1978] Loubser, J., Vanwyk, J.A., "Electron–spin resonance in study of diamond" Rep. Prog. Phys. 41(8), 1201–1248 (1978)

[Manson1996] Manson, N.B., et al., "Response of a two-level system driven by two strong fields", Phys. Rev. Lett. 76(21), 3943–3946 (1996).

[Minskey1988] Minskey, M, Scanning, 1988, 10, 128-138

[Moerner2002] Moerner, W.E., "A Dozen Years of Signle-Molecule Spectroscopy in Physics, Chemistry, and Biophysics," J. Phys. Chem. B., 106(5), 910-927 (2002)

[NielsonChuang2004] Nielsen, M.A., Chuang, I.L., Quantum Computation and Quantum Information. Cambridge University Press, New York, NY (2004)

[SalehTeich2007] Saleh, B.E.A., Teich, C.M., Fundamentals of Photonics, Wiley-Interscience, Hoboken, NJ (2007)

[Stoneman2001] Stoneham, A., Theory of Defects in Solids: Electronic Structure of Defects in Insulators and Semiconductors, Oxford University Press, Oxford. (2001)

[Tisler2009] J. Tisler et al., ACS Nano 3, 1959 (2009).

[VanOort1988] VanOort, E., et al., "Optically detected spin coherence of the diamond N–V centre in its triplet ground-state", J. Phys. C, Solid State Phys. 21(23), 4385–4391 (1988)

[VanOort1990] Vanoort E., Glasbeek, M., "Electric-field-induced modulation of spin echoes of N–V centres in diamond", Chem. Phys. Lett. 168(6), 529–532 (1990)

[Wei1995] Wei, C.J., et al., "Dressed state nutation and dynamic Stark switching", Phys. Rev. Lett. 74(7), 1083–1086 (1995)

[Windsor1998] Windsor, A.S.M., et al., "Experimental studies of a strongly driven Rabi transition", Phys. Rev. Lett. 80(14), 3045–3048 (1998)

[Zhang2004] Zhang, L.S., et al., "Coherent transient in dressed-state and transient spectra of Autler–Townes doublet", Phys. Rev. A 70(6), 063404 (2004)

Chapter 3 Spin Properties of Shallow NV centers

Note: At the time of the writing of this thesis, the majority of this chapter is taken from "Spin properties of very shallow nitrogen vacancy defects in diamond" by B. K. Ofori-Okai, S. Pezzagna, K. Chang, et al., Physical Review B 86, 081406(R) (2012). Copyright 2012 by the American Physical Society. Any reference to the supplemental refers to the supplemental to the published work.

3.1 Introduction

Isolated defect spins in solids, such as phosphorus donors in silicon [Feher1959] or the nitrogen-vacancy (NV) center in diamond [Jelezko2006], are considered important building blocks to future nanoscale devices, governed by quantum mechanics. In pure materials, defects can be so well-decoupled from their solid host that spin states approach a stability normally only found in dilute atomic vapors, including coherence times of milliseconds to seconds [Balasubramanian2009, Tyrshkin2011]. Not surprisingly, atomic defects have over the last decade attracted increasing attention motivated by their potential for spin qubits in quantum information [Kane1998, Awschalom2007] or for ultrasensitive magnetic detectors with nanometer spatial resolution [Degen2008, Maze2008, Balasubramanian2008].

The central challenge with many of these endeavors is to position the defect of interest in close proximity to other circuit elements while retaining their well-defined properties known from the bulk. On the one hand, close proximity is required for strong enough coupling. For example, for the direct coupling to nearby spin magnetic dipoles – which scales as r^{-3}, where r is distance – efficient coupling is only achieved at nanometer separations. Furthermore, for scanning magnetometry applications r directly sets the attainable spatial resolution [Degen2008]. On the other hand, the coupling will almost always happen across a material interface and defects will have to be located within nanometers from a surface, potentially destabilizing the spin and limiting its usefulness.

Several mechanisms have been found or proposed to affect the stability of shallow defects. For single donor spins in silicon, for example, the nearby Si/SiO_2 interface was shown to decrease spin coherence times even for donors tens of nanometer away due to paramagnetic impurities present at the interface [deSousa2007]. Other possible mechanisms include electric surface charge or strain fluctuations that may disturb defects through Stark and spin-orbit effects, or direct ionization [Hu2006, Rondin2010]. For nitrogen-vacancy centers in diamond, on the

other hand, rather little is currently known about the spin's performance near the surface. While functional defects have recently been reported in < 10 nm diameter nanocrystals [Tisler2009, Bradac2010] and within 3-4 nm from bulk diamond surfaces [Grotz2011] and coherence times, T_2, of tens of seconds have been observed for defects at 10 nm proximity [Gaebel2006, Maurer2010, Grinolds2011], neither a "shallowest depth" nor the involved destabilizing mechanisms are known. Given the fundamental importance of surface proximity for applications, it appears imperative to experimentally explore the limits to stability of defects at very shallow depths.

This chapter presents a systematic study of the spin resonance properties of single NV defect centers down to a proximity of about 1 nm. Defects were produced by low energy ion implantation (0.4-5 keV) and investigated by optically-detected magnetic resonance (ODMR) spectroscopy. Well-behaved defects exhibiting a narrow electron spin resonance (ESR) spectrum and coherence times exceeding 10 microseconds are observed down to the shallowest investigated depths. Additionally, an extra line broadening for defects shallower than 2 nm is observed. This broadening is compatible with the presence of surface magnetic impurities that are largely decoupled from the NV spin by motional averaging.

3.2 Sample Preparation and Characterization

A (100)-oriented single crystal of ultrapure diamond (< 5 ppb N concentration, Element Six) was used as the sample for all experiments. One sample face was implanted with $^{15}N^+$ or $^{15}N_2^+$ ions at a series of very low energies (0.4 -- 5 keV, in steps of 0.2 keV) and fluences (10^{10} – 10^{14} N/cm^2) [Pezzagna2010] (see figure 3.1). Ion implantation was carried with a 5 keV gas-source ion gun (SPECS) combined with a Wien mass filter (E × B). Ion beam direction was normal to the diamond surface with a precision of better than ± 1°. The use of molecular N2+ ions was necessary to access the lowest energies (< 2.4 keV). No difference has been found between N^+ or N_2^+ implanted defects neither in this nor in the work of [Pezzagna2010]. It is assumed that as the N2+ ion impinges the surface the molecule breaks, sending two N atoms into the bulk.

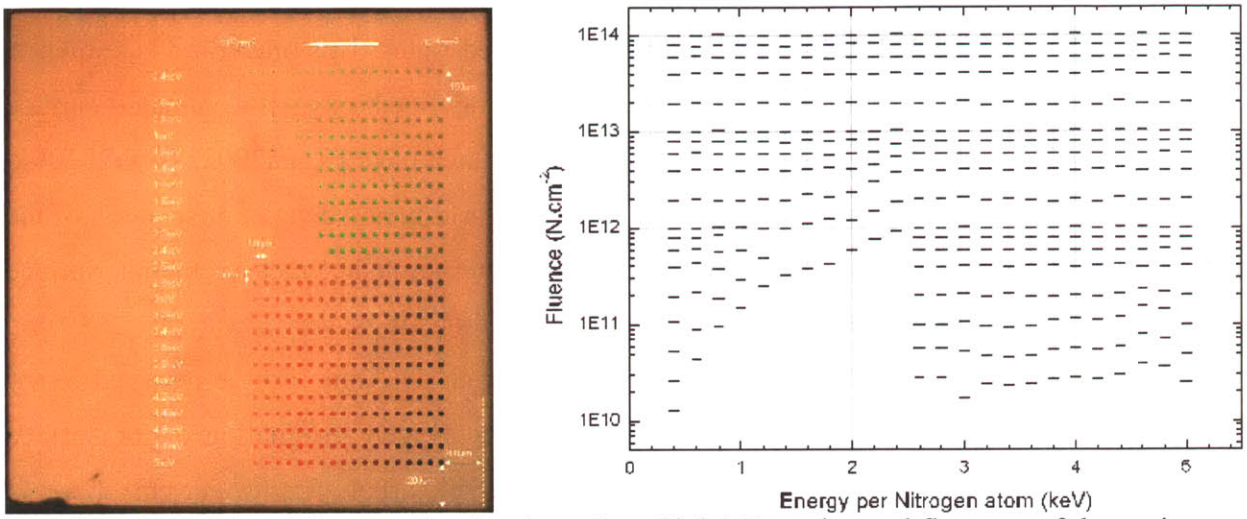

Figure 3.1. (left) Spatial map of ion implantation. (right) Energies and fluences of the various spots. The fluence is measured in nitrogen atoms/cm^2 and was adjusted for the use of N_2 versus N

Fluence was measured via the ion current, and adjusted such that each spot received the same number of ions. Thus, even if spots slightly vary in shape, the number of ions impacting the larger are of the spot is the same. The advantage of ion implantation is that the depth of created defects can be relatively accurately controlled by the implantation energy, which is important given the current lack of a direct and precise method to measure surface proximity of individual defects. To form NV centers, the sample was annealed for 2 h at 800° C and $p < 2 \times 10^7$ mbar. It is expected that nitrogen atoms do not diffuse at these temperatures because the activation energy is too high [Koga2003, Toyli2010, Ofori-Okai2012]. Diffusion coeffcients for N in diamond have been measured at higher temperatures in the context of geology and found to follow an Arrhenius relationship [Koga2003]

$$D = \left(9.7 \times 10^{-8}\right) \exp\left(\frac{0.6eV}{k_B T}\right) \quad m^2 / s \tag{3.1}$$

At T = 1100 K, the diffusion coefficient is D=3×10^{-35} m^2/s. The diffusion length for this D and for a time t = 10^4 s is $L = \sqrt{Dt} = 6 \times 10^{-16}\ m$. This is much smaller than interatomic distances (~10^{-10} m). It is possible that the vacancies created around an implanted N atom will lower the activation energy for diffusion, however, such diffusion would be confined to the local area of the N defect and would not significantly alter the N atoms position.

The sample was cleaned by boiling it for 24h under reflux in a 1:1:1 mixture of sulfuric, nitric and perchloric acid and thoroughly rinsed with purified water. This procedure is known to remove any residues (such as graphite) and to leave a well-defined, oxygen-terminated surface [Tisler2009]. We chose acid cleaning over air-oxygen-based treatment [Koga2003, Toyli2010] to avoid accidental removal of top diamond layers. We have performed a detailed inspection of the prepared diamond surface to validate the sample for later spin resonance measurements. Surface roughness was determined by atomic force microscopy and found to be very low (x_{rms} = 0.38 nm, over a 300 × 300 nm^2 window) compared to the defect depth (> 1 nm). Angle-resolved X-ray photo-electron spectroscopy (ARXPS) was used to confirm oxygen termination of the surface and absence of significant graphite residue. The absence of sp^2 carbon was further corroborated by confocal Raman spectroscopy. No difference was found between implanted and non-implanted regions.

All photoluminescence measurements were carried out on the same home-built inverted confocal microscope, except for curves presented in figure 3.4(c,d), which used a standard fluorescence microscope. NV defects were excited at 532 nm and emitted photons were filtered at an effective bandwidth of 630-800 nm and collected by an avalanche photodiode. Single center emission was confirmed by photon autocorrelation measurements like those described in chapter 2. A 40x, NA=0.95 air objective (Olympus) was used to focus the laser on to diamond sample. The sample was mounted to a motorized three-axis stage (Newport M-462-XYZ-SD) to navigate over the entire 2x2 surface of crystal. A stationary glass coverslip carrying a thin wire was inserted between objective and diamond sample for microwave excitation. This is represented schematically in figure. 3.2.

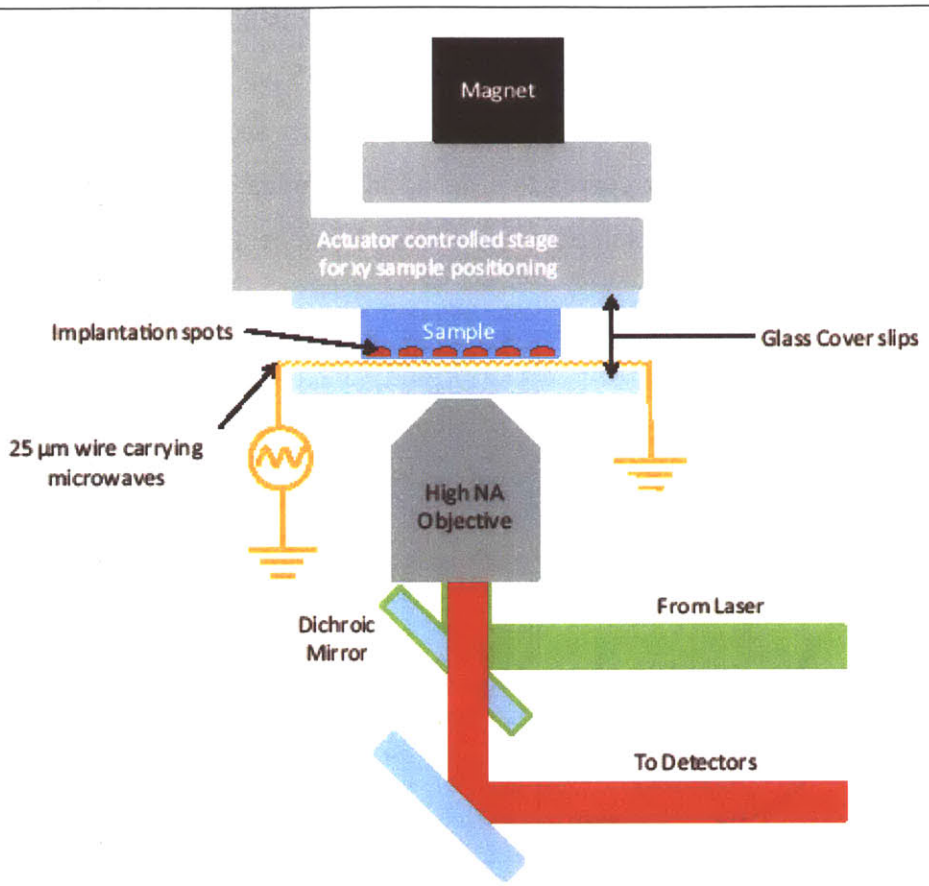

Figure 3.2. A schematic of the experimental setup used for these measurements. This is a modified version of the stationary sample geometry described in chapter 2. Here, the diamond with implanted NVs and the magnet are attached to mounts which can be positioned using motorized actuators. This allows the diamond to be suspended and helps keep the diamond surface free from debris which could ruin the surface and affect the measurement

For selective measurements of NV^0 and NV^- emission two different sets of filters with bandwidths of 582-636 nm and 660-735 nm, respectively, were used. Photoluminescence spectra were also recorded for selected implantation spots to corroborate the findings from the filter measurements (see figure 3.3). The particular choice of filters is not entirely selective to the two charge states, and the curves shown in figure 3.4(c,d) have been corrected for the overlap of these filters with the excitation spectrum. Corrected intensities were calculated using the following equation

$$\begin{pmatrix} I_{NV^0} \\ I_{NV^-} \end{pmatrix} = \begin{pmatrix} 0.44 & 0.11 \\ 0.26 & 0.66 \end{pmatrix}^{-1} \begin{pmatrix} I_{582-636} \\ I_{660-735} \end{pmatrix} \tag{3.2}$$

where the fraction of photons passing the 582-636 nm filter is 0.44 and 0.11 for NV^0 and NV^-, respectively, and the fraction of photons passing the 660-735 nm filter is 0.26 and 0.66 for NV^0 and NV^-, respectively. Numbers are calculated from the spectra given by [Rondin2010] Photoluminescence versus energy curves that do not discriminate between NV^0 and NV- were also measured using the confocal setup for the fluences numbers of 8×10^{11} cm^{-2} and 1×10^{13} cm^{-2} and gave similar results.

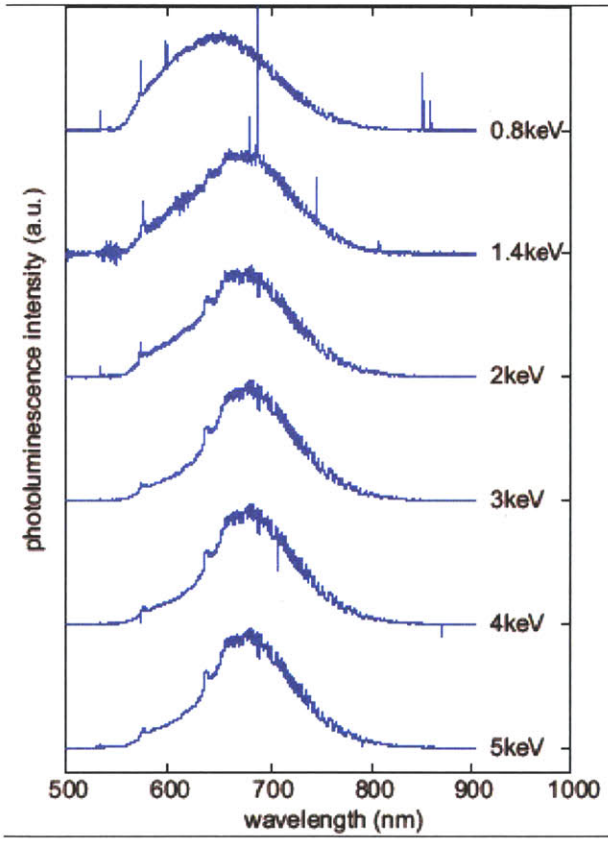

Figure 3.3. Photoluminescence spectra of selected defects at fluence 1×10^{13} cm^{-2} . Ion energy is given with each curve. Spectra are vertically offset for clarity. All cases show clear spectral signatures of both NV^0 and NV^-, namely the NV^- ZPL at 637 nm as well as the broad tail below that, which belongs to the NV^0.

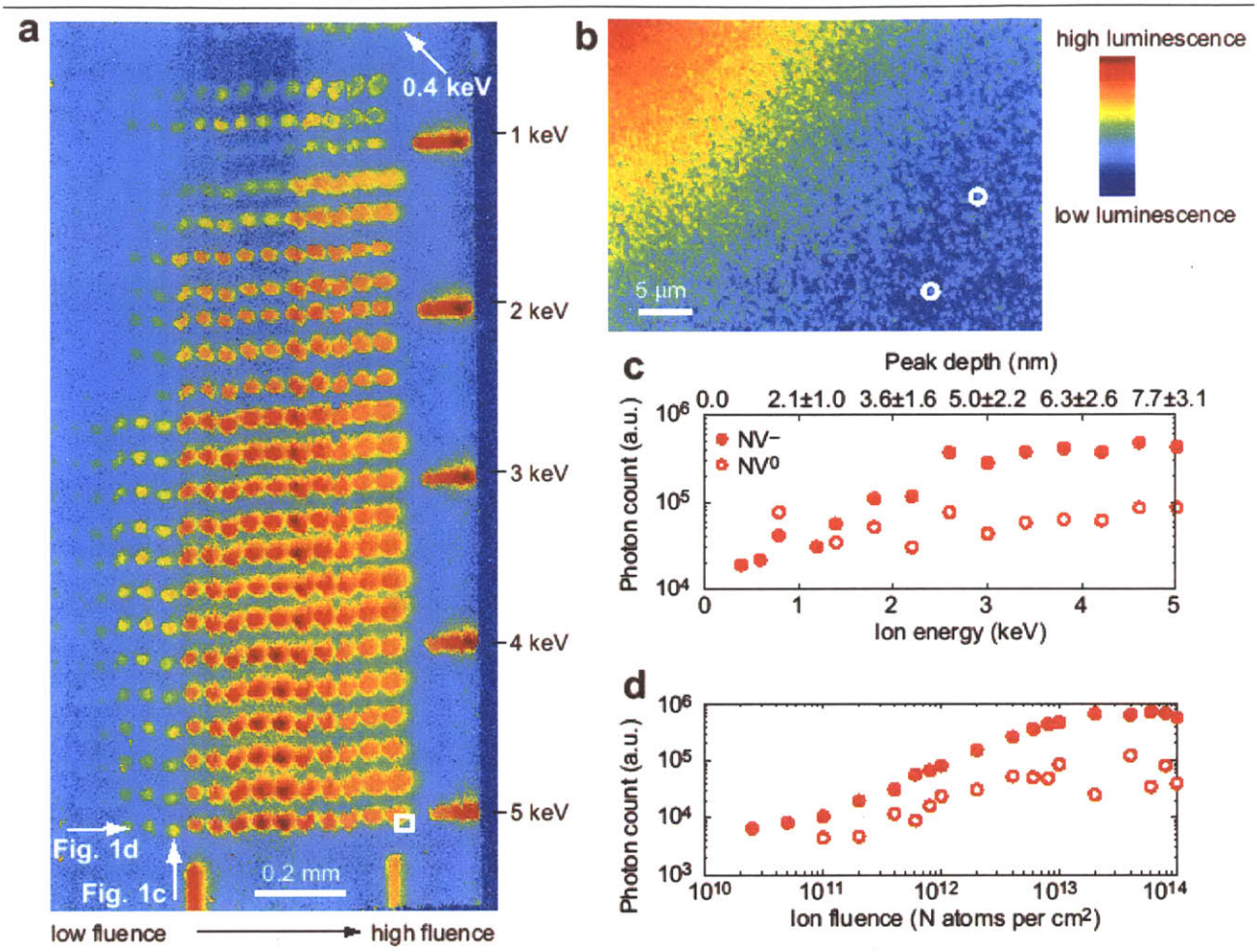

Figure 3.4. (a) Photoluminescence intensity map of the diamond surface. Shallowest 0.4-keV defects are visible at the very top. Excitation wavelength was 532 nm and detection bandwidth 630-800 nm. (b) Close up of an implantation dot at 5.0 keV (white square in (a)). Some single NV centers are encircled. (c) Luminescence intensity due to NV^- (full circles) and NV^0 (empty circles) as a function of ion energy at a fluence of 8×10^{11} cm^{-2}, measured using two pairs of filters (620-770 nm and 560-660 nm, respectively) and correcting for spectral overlap [Rondin2010]. (d) Luminescence intensity as a function of ion fluence at an energy of 5 keV.

A photoluminescence intensity map of the sample is shown in figure 3.4. Most prominently, there were optically bright NV centers are visible down to the lowest implantation energy (0.4 keV). Miscalibration of the fluence is the largest error in the photoluminescence intensities presented in figure 3.4; in particular, it is most likely responsible for the low photoluminescence of the 1-keV row. We have estimated the depth of these defects using stopping range of ions in matter (SRIM) Monte Carlo simulations [Ofori-Okai2012, Ziegler], for example, an energy of 0.4 keV corresponds to a peak depth of 1.1 ± 0.6 nm (see scale in figure

3.4(c)). SRIM calculations were shown to give suitable results of ion implantation depths over a wide energy range, including very low implantation energies [Honicke2011]. A drawback of SRIM calculations is that they are inherently statistical which is addressed below by collecting statistics on many defects.

Other important biasing effects like aperture scattering and channeling were have analyzed these effects for our study [Ofori-Okai2012]. This analysis shows that ion channeling, which can lead to depth underestimation by about a factor of 2 [Toyli2010], does not occur for ^{14}N energies below 0.6-0.7 keV and only gradually becomes more important towards higher energies. The lowest energies, where channeling is absent, are the most relevant in this study.

Figure 3.4 provides additional photoluminescence data that further corroborates this picture. We have quantitatively measured the total photoluminescence intensity as a function of energy and ion fluence and determined the relative concentrations of NV^- and NV^0 centers. In good agreement with earlier studies carried out at higher energies [Pezzagna2010] we find a monotonic decrease in total photoluminescence with decreasing energy. This monotonic decrease appears to be mostly due to a reduced concentration of NV^-, while the concentration in NV^- centers is only slightly affected. One could argue that the reduction of NV at low energies is due to a depth threshold below which the charge state becomes unstable [Rondin2010]. We have, however, not observed any photobleaching and only seen a few rare cases of fluorescence intermittency among investigated single centers [Bradac2010] that would support such a threshold. The presence of a threshold is also incompatible with the rapid changes in the spin resonance linewidth we see for the lowest energies (see below).

3.3 ODMR and Spin Echo Results

The next section of this chapter presents a study and analysis of the electron spin resonance (ESR) linewidth as a function of defect depth. ESR measurements are carried out using optically detected magnetic resonance spectroscopy. For these measurements, the fluorescence intensity from single, isolated NV center is collected while slowly sweeping an auxiliary continuous wave (cw) microwave field across the spin resonance (2.87 GHz) of the electronic ground state. Resonant microwaves induce transitions between the $m_s = 0$ and $m_s = +1$ (or $m_s = 1$) spin sublevels and lead to an up to 30% reduction in fluorescence. We use this feature to map out ESR spectra of single defects and measure their linewidth and coherence properties.

At low laser intensity (here < 1 μW) and microwave fields (a few 100 kHz Rabi frequency), linewidths below 1 MHz can be reached that are only limited by intrinsic magnetic impurities, such as nitrogen donor or nuclear ^{13}C spins.

Figure 3.5(a) collects a series of representative ESR spectra taken on NV centers at different depths. As a key feature we observe increased line broadening as NV spins are located closer to the surface. For defects deeper than 1.8 nm (0.8 keV), there is a clear hyperfine splitting due to the ^{15}N nuclear spin, but for the shallower defects at 1.5 nm (0.6 keV) and 1.1 nm (0.4 keV) depths the lines become broad and the hyperfine doublet is barely visible or entirely unresovable. This picture of broadened lines was consistent among recorded spectra (> 30 in total); for example, none of the NV centers that were 1.1 nm from the surface showed a resolved hyperfine splitting. Conversely, most 1.8 nm and all 7.7 nm defects showed a clear hyperfine doublet. All presented spectra are recorded at a single fluence (8×10^{11} cm^{-2}) and on defects that lie at the perimeter of an implantation dot, where the density is low enough to optically isolate individual NV centers and residual dipolar broadening N donor electronic spins can be excluded [Ofori-Okai2012]. The low density also ensures that implanted N atoms are far enough apart to exclude line broadening by N donor electron spins. A few spectra at higher fluence (up to 1×10^{13} cm^{-2}) were also measured and showed that the line broadening was consistent between implantation spots of the same energy but different fluence.

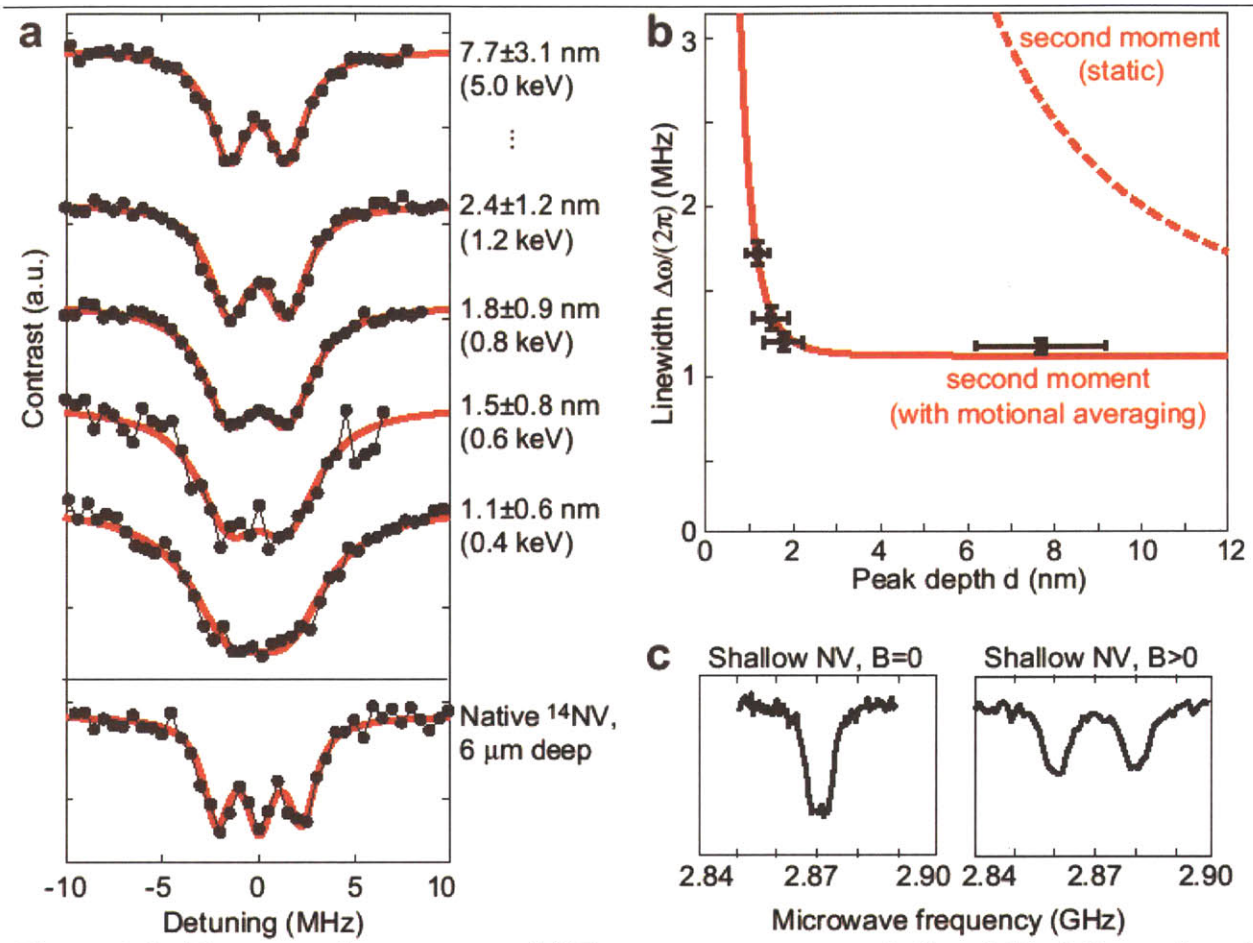

Figure 3.5. Electron spin resonance (ESR) measurements on shallow NV defect spins. (a) Representative spectra (out of > 30 total) showing increased line broadening at shallow depths. Black dots are experimental points and red solid lines are Lorentzian fits. Implanted ^{15}NV (nuclear spin I = 1/2) are distinguished from native ^{14}NV (I = 1, 99.6% natural abundance) by the different hyperfine manifold. (b) ESR linewidth $\Delta\omega/2\pi$ (half width at half height) plotted against surface proximity d. Black dots are experimental values obtained from many separately fitted curves such as the ones shown in a). Error bars denote standard error. Solid and dashed red lines are a second moment calculation with and without motional averaging taken into account, respectively. (c) Spectra of a 1.1-nm defect at zero field (top) and at 3.5 Gauss parallel bias field (bottom) rule out the presence of signicant surface strain or charge.

We have made several control measurements to ensure that the observed linebroadening is indeed a result of surface proximity. We have recorded a number of native ^{14}NV spectra at each investigated implantation spot by focusing slightly into the bulk in order to verify that broad lines were indeed a property of the defect, and not, e.g., the sample or experimental parameters. We have also measured a few spectra at higher fluence (up to 1×10^{13} cm^{-2}) and found that the line broadening did not change between implantation spots of the same energy but different

fluence. Moreover, no increase in ^{14}NV centers is seen on or near implanted areas which eliminates the possibility that ^{14}NV centers were formed from vacancies created in the ^{15}N ion tracks diffusing to ^{14}N atoms in the diamond substrate, in accordance with previous reports [Toyli2010]. Finally, we did not observe a line splitting at zero magnetic bias field, a signature for the presence of electric fields [Dolde2011] (see figure 3.5(c)), excluding the presence of significant surface strain or charge. This points towards a magnetic origin of the line broadening mechanism.

We have quantitatively analyzed the linewidth for the shallowest defects (where the pronounced changes are seen) by collecting and fitting a number of individual spectra and averaging the resultant linewidth parameter as shown in figure 3.5(b). In order to determine an accurate mean number for the linewidth at various implantation energies, over 30 spectra were collected and individually fitted. Line width parameters $\Delta\omega$ (0.5 × FWHH) for the ODMR spectra were estimated by fitting a Lorentzian to each of the hyperfine split lines. For ^{15}NV, the fit function used is

$$I(\omega) = I_0 \left(1 - c \left[\frac{1}{\left(\frac{\omega - \omega_0 + a/2}{\Delta\omega} \right)^2 + 1} + \frac{1}{\left(\frac{\omega - \omega_0 - a/2}{\Delta\omega} \right)^2 + 1} \right] \right) \tag{3.3}$$

In this equation, ω is the microwave frequency, and I_0, c, ω_0, and $\Delta\omega$ are free fit parameters that correspond to the intensity, the contrast, the center position of the ODMR line, and the linewidth (all in units of angular frequency). $a/(2\pi)$ = 3.0 MHz is the hyperfine splitting and was assumed a fixed parameter.

In the following we attempt to explain the surface-induced line broadening by the presence of paramagnetic impurities. Surface impurities have been found at substantial density for clean, oxygen-terminated nanodiamonds [Tisler2009]. These nanodiamonds underwent the same surface cleaning procedure and are thus expected to have the same surface chemistry as our diamond substrate. We model surface impurities by assuming a homogeneous, two-dimensional dipolar bath of electron spins (S = 1/2) with an areal density of $\rho_A \approx 10$ spins/nm^2 [Tisler2009], similar to the sketch in figure 3.6.

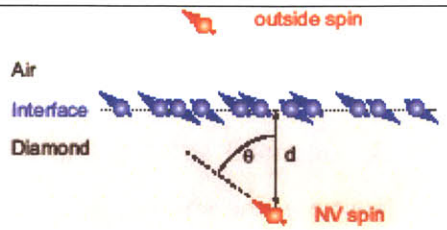

Figure 3.6. Sketch of a nitrogen-vacancy defect spin near a paramagnetic surface impurity layer, as described in the text. *d* and θ denote distance and orientation of the defect spin to the interface plane, and quantization is along N-V axis. A potential target spin, representative for sensing applications, is also shown.

In the following we use the theory of moments developed in [Slichter1990] to analyze our results, but note that a parallel framework has been developed for T_1 and T_2 values in the context of paramagnetic impurities in the Si/SiO_2 interface [deSousa2007]. The second moment $\langle \Delta\omega^2 \rangle_d$ ($\langle \Delta\omega^2 \rangle_d \approx \Delta\omega_d^2$ where $\Delta\omega_d^2$ is the linewidth) of an electron spin S due to a quasi-continuous, two-dimensional layer of electron spins I = 1/2 with density ρ_A is given by

$$\langle \Delta\omega^2 \rangle_d = \frac{1}{3}\frac{\mu_0}{(4\pi)^2}\gamma_I^2\gamma_S^2\hbar^2 S(S+1)\int_{layer}\rho_A\frac{(3\cos^2\theta-1)^2}{r^6}dxdy \tag{3.4}$$

$$= \frac{1}{4}\frac{\mu_0}{(4\pi)^2}\gamma^4\hbar^2 S(S+1)\int_{layer}\rho_A\frac{(3\cos^2\theta-1)^2}{r^6}dxdy \tag{3.5}$$

where $\gamma_I = \gamma_S = \gamma = 2\pi \times 2.8 \times 10^{10}$ Hz/T is the electron gyromagnetic ratio, $\mu_0 = 4 \times 10^{-7}$ Vs/(Am) and r and θ the distance and angle, respectively, between the NV axis and a surface spin. This second moment has units of angular frequency squared. In the following it is assumed that a small bias field B_0 is applied along the NV axis and that all surface spins are aligned with this field. By performing the following substitutions

$$r(x,y,z) = \sqrt{x^2+y^2+z^2} \tag{3.6}$$

$$\cos(\theta) = \left[\frac{x}{r}\sin(\theta_0) + \frac{z}{r}\cos(\theta_0)\right] \tag{3.7}$$

where z = d is the distance between spin S and the surface layer, and θ_0 is the angle between NV axis and surface normal, integration of equation 3.5 gives

$$\left\langle \Delta\omega^2 \right\rangle_d = \frac{3\hbar^2 \mu_0^2 \rho_A \gamma^4}{2048\pi d^4} \times \left(3 + 2\cos^2(\theta_0) + 3\cos^4(\theta_0)\right) \tag{3.8}$$

For an NV center near a (100) surface (θ_0 = 54.7°), $3 + 2\cos^2(\theta_0) + 3\cos^4(\theta_0) = 4$. The overall linewidth parameter $\Delta\omega$ that can be directly compared to experimental data is given by

$$\Delta\omega = \left[\Delta\omega_0^2 + \left\langle \Delta\omega^2 \right\rangle_d\right]^{\frac{1}{2}} = \Delta\omega_0 \left[1 + \frac{d_0^4}{d^4}\right]^{\frac{1}{2}} \tag{3.9}$$

where $\Delta\omega_0$ is the intrinsic linewidth. d_0 is an empirical "critical distance", $d_0^4 = 3\hbar^2 \mu_0^2 \rho_A \gamma^4 / 512\pi \left\langle \Delta\omega^2 \right\rangle_0$, that represents the separation below which the surface contribution to the linewidth dominates. A fit to equation 3.9 yields d_0 =1.3 ± 0.2 nm and $\Delta\omega/(2\pi)$=1.1 ± 0.1 MHz. The error in d_0 both contains the fit error and straggling uncertainty.

The calculated linewidth $\Delta\omega$ and the corresponding experimental values are compared in figure 3.5(b). The linewidth predicted by the model (dashed line) is about 30 larger than the one experimentally observed. In fact, the second moment calculation suggests that substantial line broadening would already be expected for defects deeper than 10 nm. This is clearly not the case. One could try and attribute the discrepancy to a lower defect density (requires about 1000 × lower ρ_A), or a miscalibration of implantation depth (by 5.5). Given the order of magnitude difference, either assumption or even a combination of them appears unlikely.

An alternative argument which can be made is that the reduced linewidth is caused by motional averaging through fast reorientations of surface spins. Rapid fluctuations within the spin bath are known to suppress the line broadening as $\left\langle \Delta\omega^2 \right\rangle_d' = \left(\left\langle \Delta\omega^2 \right\rangle_d \tau_c\right)^2$ where $\tau_c << \left\langle \Delta\omega^2 \right\rangle_d^{1/2}$ is the correlation time of fluctuations and $\left\langle \Delta\omega^2 \right\rangle_d$ is the static linewidth given by Eq. (1) [Kubo1954]. In order to interpret the experimental data of figure 3.5(b) using this modified dynamic linewidth one needs to assume a correlation time of about $\tau_c \approx$ 10 ns (solid line in the figure). This correlation time is in good agreement with spin-lattice relaxation times T_1 observed for paramagnetic centers in amorphous carbon [Barklie2000], sintered detonation nanodiamonds [Baranov2011] and in the typical range of spin-lattice relaxation times T_1 observed for free radicals.

Finally, we have also measured echo decay times of several 0.4 keV (1.1 nm) defects to establish a lower bound for the coherence times T_2 of very shallow spins. Coherence times were measured using a Hahn echo sequence with equal free evolution times $\tau'=\tau$ before and after the central π pulse. This pulse sequence produces the decay of the echo maximum. The echo decay curves were fitted by the equation following equation (adapted from [Childress2006]),

$$I(t) = A\exp\left[-\frac{(2t)^{n_1}}{T_2^3}\right]\times\sum_{k=0}^{N}\exp\left[-\frac{(t-k\tau_r)^{n_2}}{(2\tau_c)^2}\right]+C \qquad \begin{matrix}(3.10)\\(2.23)\end{matrix}$$

where τ_c describes the fast initial decay caused by the fluctuating ^{13}C nuclear spin bath, and T_2 reflects the slower decay of the "echo revivals" appearing at the periodicity τ_r of the ^{13}C Larmor precession. Here, $n_1 = 3$ and $n_2 = 2$ while A, C, τ_c, τ_r, and T_2 are free fit parameters. N was adjusted to match the number of revivals seen. Additionally, fitting with arbitrary values for n_1 and n_2 was also attempted, but fits would either not converge or yielded the same values for τ_c and T_2 within experimental error. Thus, no conclusion can be drawn on the exponent. In principle, the T_2 decay exponential will change from $n_1 = 3$ to $n_1 = 1$ for a rapidly fluctuating environment (such as caused by fast reorientation of surface spins), but from the present data we cannot favor one over the other.

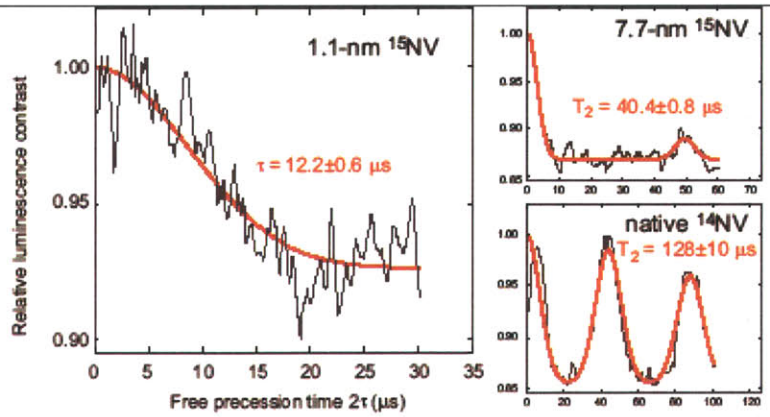

Figure 3.7 Hahn-echo decay of a 1.1-nm NV center and, for comparison, for a 7.7-nm and a native defect. Black curves are experimental data and red lines are t according to [Childress2006]

A representative Hahn echo decay curve with an echo decay time of $\tau = 12$ µs is shown in figure 3.7; other defects at the same depth showed values between 7 and 12 µs. Given the Gaussian decay profile we suspect that the echo decay is, however, dominated by the slowly fluctuating ^{13}C nuclear spin environment intrinsic to diamond [Childress2006] rather than by

rapidly fluctuating surface impurities, where one would expect an exponential decay. Consequently, one can conclude that $T_2 > 10$ μs.

Given the shallow depths of the investigated NV centers it is instructive to extrapolate their magnetic moment sensitivity, which is the key figure of merit for the sensing of external spins and future applications to nanoscale magnetic resonance imaging and spectroscopy [Degen2008]. For example, taking an echo decay time 12 μs, a photon count rate of C = 0.0018 photons/shot and an optical contrast between ms = 0 and ms = 1 states of ε = 7% (1.1-nm defect in figure 3.7(a)), we find an optimal ac magnetic field sensitivity of $B_{\min} \approx \left(0.5\pi\gamma\varepsilon\sqrt{\tau_c}\right)^{-1} \sim 2.2\mu T/\sqrt{Hz}$ [Taylor2008]. Here, the relevant (most susceptible) ac frequency is set by the inverse of the echo du- ration, i.e., tens of kHz. For a magnetic moment located directly on the surface and taking into account the angle of the NV spin, this sensitivity equates to a minimum detectable magnetic moment of $\mu_{\min} \sim 4\pi d^3 B_{\min}/0.96\mu_0\mu_B \sim 0.003\mu_B/\sqrt{Hz}$ where μ_B is the Bohr magneton. For dc signal detection, the corresponding magnetic field and moment sensitivities are $B_{\min} \approx 8\Delta\omega_0/\left(3\sqrt{3}\gamma\varepsilon\sqrt{I_0}\right) \sim 19\mu T/\sqrt{Hz}$ and $\mu_{\min} \sim 0.03\mu_B/\sqrt{Hz}$, respectively, where $I_0 = 2 \times 10^3$ photons/s is the cw photon count rate and ε = 11 % taken from the data in figure 3.5. Even if our depth calibration were off by a factor of 2, which is not likely but possible given the large uncertainty of implantation depth, $\mu_{\min}$ would still equate to $0.03\mu_B/\sqrt{Hz}$ (ac) and $0.2\mu_B/\sqrt{Hz}$ (dc), respectively.

In conclusion, we have investigated spin and optical properties of single nitrogen vacancy defects in diamond at very shallow depths. Functional defects are found down to about 1 nm, and significant broadening of the electron spin resonance is only observed for defects < 2 nm. This surface stability is unmatched by other solid-state spin systems, such as phosphorus donors in silicon or semiconductor quantum dots, and a key requirement for a number of anticipated quantum and sensing applications. In particular, we have inferred a sensitivity to outside magnetic moments (such as surface electron and nuclear spins) that extends down to $< 0.01\mu_B/\sqrt{Hz}$. Such a sensitivity is currently unreached by any existing magnetic sensor and might, if combined with the imaging capabilities of a scanning probe apparatus [Degen2008, Taylor2008], enable the direct mapping of single nuclear spins in molecules and thin films with chemical specificity and nanometer spatial resolution.

There were many people who were influential in this work. G. Balasubramanian, H. Balch, J. Hodges, L. Robledo, and C. Ryan were helpful in constructing the optical setup, and A. Rossi and J. Stadler for help with surface inspection.

References:

[Awschalom2007] Awschalom, D.D., Epstein, R., and Hanson, R., "The Diamond Age of Spintronics", Scientific American 297, 84 (2007).

[Balasubramanian2008] Balasubramanian, G., et al., "Nanoscale imaging magnetometry with diamond spins under ambient conditions" Nature 455, 648 (2008).

[Balasubramanian2009] Balasubramanian, G., et al., "Ultralong spin coherence time in isotopically engineered diamond" Nature Materials 8, 383 (2009).

[Baranov2011] Baranov, P.G., et al., "Enormously High Concentrations of Fluorescent Nitrogen-Vacancy Centers Fabricated by Sintering of Detonation Nanodiamonds", Small 7, 1533-1537 (2011).

[Barklie2000] Barklie, R.C., Collins, M., Silva, S.R.P., "EPR linewidth variation, spin relaxation times, and exchange in amorphous hydrogenated carbon", Phys. Rev. B 61, 3546-3554 (2000).

[Bradac2010] Bradac, C., et al., "Observation and control of blinking nitrogen-vacancy centres in discrete nanodiamonds" Nat. Nanotechnol. 5, 345-349 (2010).

[Chernobrod2005] Chernobrod, B.M., Berman, G.P., "Spin microscope based on optically detected magnetic resonance", J. Appl. Phys. 97, 014903 (2005)

[Childress2006] Childress, L., et al. "Coherent dynamics of coupled electron and nuclear spin qubits in diamond", Science 314, 281 (2006)

[Degen2008] Degen, C.L., "Scanning magnetic field microscope with a diamond single-spin sensor", Appl. Phys. Lett. 92, 243111 (2008).

[deSousa2007] R. de Sousa, "Dangling-bond spin relaxation and magnetic 1/f noise from the amorphous-semiconductor/oxide interface: Theory" Phys. Rev. B 76, 245306 (2007).

[Dolde2011] Dolde, F., et al., "Electric-field sensing using single diamond spins" Nat. Phys. 7, 459-463 (2011).

[Feher1959] Feher, G., "Electron Spin Resonance Experiments on Donors in Silicon. I. Electronic Structure of Donors by the Electron Nuclear Double Resonance Technique" Phys. Rev. 114, 1219-1244 (1959).

[Gaebel2006] Gaebel, T., et al., "Room-temperature coherent coupling of single spins in diamond", Nature Physics 2, 408 (2006).

[Grinolds2011] Grinolds, M.S., et al., "Quantum control of proximal spins using nanoscale magnetic resonance imaging", Nat Phys 7, 687-692 (2011).

[Grotz2011] Grotz, B., et al., "Sensing external spins with nitrogen-vacancy diamond", New J. Phys. 13, 055004 (2011).

[Honicke2011] Honicke, P., et al., "Depth profile characterization of ultra shallow junction implants", Anal. Bioanal. Chem. 396, 2825-283 (2010).

[Hu2006] Hu, X., and das Sarma, S., "Charge-Fluctuation-Induced Dephasing of Exchange-Coupled Spin Qubits" Phys. Rev. Lett. 96, 100501 (2006).

[Jelezko2006] Jelezko, F., Wrachtrup, J., "Single defect centres in diamond: A review" Phys. Stat. Sol. (a) 203. 3207 (2006).

[Kane1998] Kane, B., "A silicon-based nuclear spin quantum computer" Nature 393, 133-137 (1998).

[Koga2003] Koga, K.T., van Orman, J.A., Walter, M.J., "Diffusive relaxation of carbon and nitrogen isotope heterogeneity in diamond: a new thermochronometer", Phys. Earth Planet. Inter. 139, 35-43 (2003).

[Kubo1954] Kubo, R., Tomita, K., "A General Theory of Magnetic Resonance Absorption", J. Phys. Soc. Jpn. 9, 888-919 (1954).

[Maurer2010] Maurer, P.C., et al., "Far-field optical imaging and manipulation of individual spins with nanoscale resolution", Nat Phys 6, 912-918 (2010).

[Maze2008] Maze, J.R.., et al., "Nanoscale magnetic sensing with an individual electronic spin in diamond" Nature 455, 644 (2008).

[Ofori-Okai2012] See Supplementary Material to the published manuscript.

[Pezzagna2010] Pezzagna, S., et al., "Creation efficiency of nitrogen-vacancy centres in diamond", New J. Phys. 12, 065017 (2010).

[Rondin2010] Rondin, L., et al., "Surface-induced charge state conversion of nitrogen-vacancy defects in nanodiamonds" Phys. Rev. B 82, 115449 (2010).

[Slichter1990] Slichter, C. P., Principles of Magnetic Resonance, 3rd edition, Springer, Berlin, (1990)

[Taylor2008] Taylor, J.M., et al., "High-sensitivity diamond magnetometer with nanoscale resolution" Nature Physics 4, 810 (2008).

[Tisler2009] Tisler, J., et al., "Fluorescence and Spin Properties of Defects in Single Digit Nanodiamonds" ACS Nano 3, 1959 (2009).

[Toyli2010] Toyli, D.M., et al., "Chip-Scale Nanofabrication of Single Spins and Spin Arrays in Diamond", Nano Lett. 10, 3168-3172 (2010).

[Tyrshkin2011] Tyryshkin, A.M., et al., "Electron spin coherence exceeding seconds in high-purity silicon" Nature Mat. 11, 143-147 (2011).

[Ziegler] Ziegler, J. F., Biersack, J. P., Ziegler, M. D.. "SRIM, the stopping and range of ions in matter", http://srim.org.